FeMo Cofactor of Nitrogenase: A Density Functional Study of States M^N, M^{OX}, M^R, and M^I

Timothy Lovell,* Jian Li,† Tiqing Liu, David A. Case,* and Louis Noodleman*

Contribution from the Department of Molecular Biology TPC-15, The Scripps Research Institute, La Jolla, California 92037

Received July 31, 2001. Revised Manuscript Received September 28, 2001

Abstract: The M^N $S = {}^3/_2$ resting state of the FeMo cofactor of nitrogenase has been proposed to have metal-ion valencies of either $Mo^{4+}6Fe^{2+}Fe^{3+}$ (derived from metal hyperfine interactions) or $Mo^{4+}4Fe^{2+}3Fe^{3+}$ (from Mössbauer isomer shifts). Spin-polarized broken-symmetry (BS) density functional theory (DFT) calculations have been undertaken to determine which oxidation level best represents the M^N state and to provide a framework for understanding its energetics and spectroscopy. For the $Mo^{4+}6Fe^{2+}Fe^{3+}$ oxidation state, the spin coupling pattern for several spin state alignments compatible with $S = {}^3/_2$ were generated and assessed by energy and geometric criteria. The most likely BS spin state is composed of a Mo3Fe cluster with spin $S_a = 2$ antiferromagnetically coupled to a 4Fe′ cluster with spin $S_b = {}^7/_2$. This state has a low DFT energy for the isolated FeMoco cluster and the lowest energy when the interaction with the protein and solvent environment is included. This spin state also displays calculated metal hyperfine and Mössbauer isomer shifts compatible with experiment, and optimized geometries that are in excellent agreement with the protein X-ray data. Our best model for the actual spin-coupled state within FeMoco alters this BS state by a slight canting of spins and is analogous in several respects to that found in the 8Fe P-cluster in the same protein. The spin-up and spin-down components of the LUMO contain atomic contributions from Mo^{4+} and the homocitrate and from the central prismane Fe sites and μS^2 atoms, respectively. This qualitative picture of the accepting orbitals for M^N is consistent with observations from Mössbauer spectra of the one-electron reduced states. Similar calculations for the $Mo^{4+}4Fe^{2+}3Fe^{3+}$ oxidation state yield results that are in poorer agreement with experiment. Using the $Mo^{4+}6Fe^{2+}Fe^{3+}$ oxidation level as the most plausible resting state, the geometric, electronic and energetic properties of the one-electron redox transition to the oxidized state, M^{OX}, catalytically observed M^R and radiolytically reduced M^I states have also been explored.

1. Introduction

Iron−sulfur proteins play a significant role in biological electron transfer and have been an important part of all living organisms for the last two or three billion years.[1] Following initial recognition of these proteins some thirty years ago, their physical properties have now been studied using a wide variety of spectroscopic and theoretical techniques[2] and the biological importance of iron−sulfur (Fe−S) clusters is well-documented. Aside from their role as electron-transfer agents,[3] Fe−S clusters function as integral components of complex multielectron oxidoreductase proteins,[4] where substrate binding and catalytic transformations are often accompanied by the multiple transfer of electrons, as in the sulfite[5] and nitrite[6] reductases and several hydrogenases.[7] Fe−S clusters also play a critical functional role in the redox-active metalloenzyme, nitrogenase.

The biological conversion of dinitrogen (N_2) into ammonia (NH_3) by nitrogenase constitutes a key component of the nitrogen cycle,[8,9] in which nitrogen availability to support life on earth is maintained. Within the cycle, prokaryotic microorganisms reduce dinitrogen first to ammonia under mild physiological conditions, which subsequently is used for constructing the essential amino acid building blocks for the synthesis of proteins and nucleic acids. Nitrogen fixation is frequently the limiting factor in plant growth, and consequently, industrial processes have been developed[10] to fix dinitrogen chemically.

Nitrogenases are known with either purely Fe or with VFe-containing proteins,[11] but the best-studied and most prevalent is a molybdenum−iron-based system, whose biochemistry has been extensively reviewed.[12] Molybdenum−iron nitrogenase consists of two separate proteins: the Fe protein and the MoFe

* To whom correspondence should be addressed. E-mail: tlovell@scripps.edu, case@scripps.edu, and lou@scripps.edu. Fax: +1 858 784 8896.

† Present Address: Texas Biotechnology Corporation, 7000 Fannin Street, Houston, TX 77030.

(1) (a) Beinert, H. *FASEB J.* **1990**, *4*, 2483. (b) Beinert, H. *J. Biol. Inorg. Chem.* **2000**, *5*, 2.

(2) (a) Lovenberg, W., Ed.; *Iron-Sulfur Proteins*; Academic Press: New York, 1973; 1977; Vols. I, II, and III. (b) *Advances in Inorganic Chemistry*; Cammack, R., Ed.; Academic Press: New York, 1992; Vol. 38.

(3) (a) Mitchell, P. J. *Biochemistry* 1985, *97*, 1. (b) Han, A. L.; Yagi, T.; Hatefi, Y. *Arch. Biochem. Biophys.* **1989**, *275*, 166.

(4) Spiro, T. G., Ed. *Iron Sulfur Proteins*; Academic Press: New York, 1981.

(5) Crane, B. R.; Getzoff, E. D. *Curr. Opin. Struct. Biol.* **1996**, *6*, 744.

(6) Crane, B. R.; Siegel, L. M.; Getzoff, E. G. *Science* **1995**, *270*, 59.

(7) Adams, M. W. W.; Stiefel, E. I. *Science* **1998**, *282*, 1842.

(8) (a) Stacey, G.; Burris, R. H.; Evans, H. J. *Biological Nitrogen Fixation*; Chapman and Hall: New York, 1992. (b) Steifel, E. I.; Concouvanis, D.; Newton, W. E. *Molydenum Enzymes, Cofactors, and Model Systems*; American Chemical Society: Washington, DC, 1993. (c) Holm, R. H.; Kennepohl, P.; Solomon, E. I. *Chem. Rev.* **1996**, *96*, 2239.

(9) (a) Burgess, B. K.; Lowe, D. J. *Chem. Rev.* **1996**, *96*, 2983 and references therein. (b) Ferguson, S. J.; *Curr. Opin. Chem. Biol*., **1998**, *2*, 182.

(10) (a) Tennison, S. R. In *Catalytic Ammonia Synthesis Fundamentals and Practice*; Jennings, J. R., Ed.; Plenum Press: New York, 1991; p 303. (b) Howard, J. B.; Rees, J. B. *Chem. Rev.* **1996**, *96*, 2965. (c) Rawls, R. L. *Chem. Eng. News* **1998**, 29. (d) Sellmann, D.; Sutter, J. *Acc. Chem. Res.* **1997**, *30*, 460.

(11) Eady, R. R. *Chem. Rev.* **1996**, *96*, 3013.

10.1021/ja011860y CCC: $20.00
Published on Web 11/16/2001

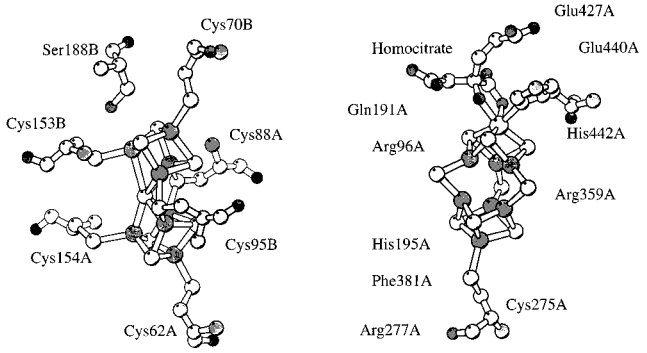

Figure 1. Structures of the "P" cluster (left) and "M" center or FeMo cofactor (right) of the MoFe protein. Protein residues surrounding each cluster are also indicated. Figure 1 was prepared using MOLSCRIPT: Kraulis, P. J. *J. Appl. Crystallogr.* **1991**, *24*, 946.

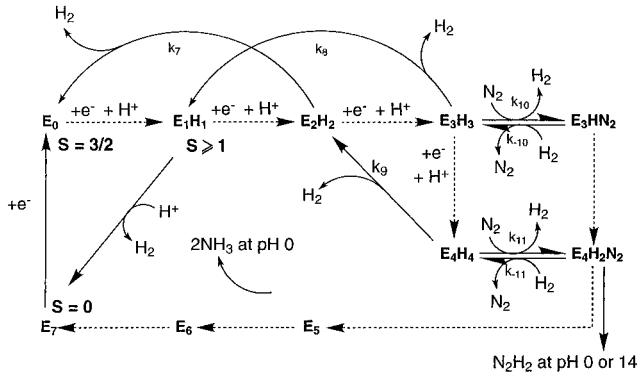

Figure 2. The Lowe−Thorneley proposed catalytic cycle of nitrogenase (modified from original version).

protein, named according to their metal composition.[13] The Fe protein contains a single 4Fe4S cluster, similar to that observed for other iron−sulfur proteins. The MoFe protein contains two unique types of polynuclear metal−sulfur clusters, the P-cluster (Figure 1, left) and the FeMo cofactor (alternatively M center or FeMoco) (Figure 1, right), the former containing eight iron atoms and the latter comprising one molybdenum and seven iron sites. The docking of the MgATP bound form of the Fe protein to the MoFe protein initiates enzyme turnover, during which the role of the Fe protein is to transfer electrons via the P-cluster to the active FeMo cofactor, which is the proposed site of binding and reduction of dinitrogen. The overall chemical reaction stoichiometry (assuming the product distribution of N_2:H_2 is 1:1) is:

$$N_2 + 8H^+ + 8e^- + 16\text{MgATP} \rightarrow 2NH_3 + H_2 + 16\text{MgADP} + 16P_i$$

and for efficient turnover this process requires the hydrolysis of *at least* two units of MgATP for each electron transferred. Another major determinant of product distribution is the electron flux through the MoFe protein. High flux favors reduction of N_2 while at very low flux, dihydrogen (H_2) is the only product even in the presence of N_2.

The activity of nitrogenase is generally described in terms of the catalytic cycle proposed by Lowe and Thorneley, in which *Klebsiella pneumoniae* nitrogenase has been analyzed in terms of a kinetic scheme describing the different protonation and oxidation states of the MoFe protein[14a] (Figure 2). In brief, successive one-electron reductions of the resting FeMoco (denoted E_0) give $1e^-$, $2e^-$, and $3e^-$ reduced states labeled as E_1, E_2, and E_3, etc., while coupled proton transfers, one for each electron transferred to the cluster, give states E_1H_1, E_2H_2, and E_3H_3, etc. Beyond state E_3H_3, an extensive accumulation of kinetic data supports N_2 entering the cycle and binding as part of the process by which N_2 and H_2 exchange.[9] The eventual cleavage of the dinitrogen triple bond and dissociation of two molecules of NH_3 results after step $E_4H_2N_2$, and the cycle proceeds via another intermediate state, E_7, back to the resting state. State E_7 is presumed to be one electron more oxidized than the resting E_0 state and is probably similar to a diamagnetic state characterized by spectroscopy.[15,16]

A key advance to understanding nitrogenase function in terms of the proposed kinetic scheme has been provided by the crystal structures of both the Fe protein and the MoFe protein,[17] the latter being the central focus of this study. Crystal structures of the MoFe protein have been isolated from several independent bacteria, such as *Azotobacter vinelandii* (*Av*),[13,17a−c] *Clostridium pasteurianium* (*Cp*)[17e] and *Klebsiella pneumoniae* (*Kp*).[17g] EPR studies on the *Av* crystals give rise to the spectroscopically assigned native dithionite-reduced (P^N, M^N) and oxidized (P^{OX}, M^{OX}) states. Electrochemical and spectroscopic studies[9,13,18] further reveal that each M^{OX} cluster is one electron oxidized compared to M^N; each P^{OX} cluster is two electrons oxidized with respect to P^N.

The structure of the M-center, the proposed active site of nitrogenase (Figure 1, right) features two distorted metal cubane fragments linked by three μ-2 sulfide bridges. One cubane has four iron centers (4Fe3S), the other comprises three iron sites and one molybdenum (Mo3Fe3S), with each cuboidal component attached to the protein via only one ligand. Cys275·Sγ coordinates to the corner Fe site of the 4Fe3S cubane to complete its tetrahedral environment, while His442·Nδ provides the covalent link to the Mo site, whose pseudooctahedral coordination sphere is completed by carboxylate and hydroxyl oxygens of an endogenous organic homocitrate ligand. Contrary to initial expectations, the availability of the FeMoco structure has yielded only limited insight into cofactor function and underlying electronic structure. A more complete understanding has been hindered by the limited availability of definitive experimental data, which thus far have derived from a variety of biochemical experiments, genetics techniques, kinetics

(12) (a) Rees, D. C. *Curr. Opin. Struct. Biol.* **1993**, *3*, 921. (b) Rees, D. C.; Chan, M. K.; Kim, J. *Adv. Inorg. Chem.* **1993**, *40*, 89. (c) Smith, B. E. *Adv. Inorg. Chem.* **1999**, *47*, 159.

(13) Peters, J. W.; Stowell, M. H. B.; Soltis, S. M.; Finnegan, M. G.; Johnson, M. K.; Rees, D. C. *Biochemistry* **1997**, *36*, 1181.

(14) (a) Thorneley, R. N. F.; Lowe, D. In *Molybdenum Enzymes*; Spiro, T. G., Ed.; Wiley-Interscience: New York, 1985. (b) Thorneley, R. N. F.; Lowe, D. *J. Biol. Inorg. Chem.* **1996**, *1*, 576.

(15) (a) Huynh, B. H.; Münck, E.; Orme-Johnson, W. H. *Biochim. Biophys. Acta* **1979**, *527*, 192. (b) Huynh, B. H.; Henzel, M. T.; Christner, J. A.; Zimmermann, R.; Orme-Johnson, W. H.; Münck, E. *Biochim. Biophys. Acta* **1980**, *623*, 124.

(16) Johnson, M. K.; Thomson, A. J.; Robinson, A. E.; Smith, B. E. *Biochim. Biophys. Acta* **1981**, *671*, 61.

(17) (a) Kim, J.; Rees, D. C. *Nature* 1992, *360*, 553. (b) Kim, J.; Rees, D. C. *Science* **1992**, *257*, 1677. (c) Chan, M. K.; Kim, J.; Rees, D. C. *Science* **1993**, *260*, 792. (d) Georgiadis, M. M.; Komiya, H.; Woo, D.; Kornuc, J. J.; Rees, D. C. *Science* **1992**, *257*, 1653. (e) Kim, J.; Woo, D.; Rees, D. C. *Biochemistry* **1993**, *32*, 7104. (f) Bolin, J. T.; Ronco, A. E.; T. V.; Morgan, T. V.; Mortenson, L. E.; Xuong, N. *Proc. Natl. Acad. Sci. U.S.A.* **1993**, *90*, 1078. (g) Mayer, S. M.; Lawson, D. M.; Gormal, C. A.; Roe, S. M.; Smith, B. E. *J. Mol. Biol.* **1999**, *292*, 871. (h) Schindelin, N.; Kisker, C.; Schlessman, J. L.; Howard, J. B.; Rees, D. C. *Nature* **1997**, *387*, 370. (i) Strop, P.; Takahara, P. M.; Chiu, H.-J.; Angove, H. C.; Burgess, B. K.; Rees, D. C. *Biochemistry* **2001**, *40*, 651.

(18) (a) Zimmermann, R.; Münck, E.; Brill, W. J.; Shah, V. K.; Henzyl, M. T.; Rawlings, J.; Orme-Johnson, W. H. *Biochim. Biophys. Acta* **1978**, *537*, 185. (b) Surerus, K. K.; Hendrich, M. P.; Christie, P. D.; Rottgardt, D.; Orme-Johnson, W. H.; Münck, E. *J. Am. Chem. Soc.* **1992**, *114*, 8579.

measurements and spectroscopic (EPR, Mössbauer, ENDOR, and EXAFS) studies.[9]

Isolation of the MoFe protein in the presence of excess dithionite reveals an M-center in the resting oxidation state that yields a prominent $S = {}^3/_2$ EPR signal at $g = 4.32$, 3.68, and 2.01.[19] An analysis of the oxidation states of the individual Fe sites has, however, been prevented by the difficulties associated with interpretation of the hyperfine parameters from the ENDOR[20] and Mössbauer data.[15] Combined ^{57}Fe Q-band ENDOR and EPR data suggest metal valence assignments of $1Mo^{4+}$, $6Fe^{2+}$, and $1Fe^{3+}$ (alternatively $1Mo^{4+}$, $5Fe^{2+}$, and $2Fe^{2.5+}$).[19,20] These valence assignments have recently come under scrutiny following a revision of the original Mössbauer data analysis[21] and $1Mo^{4+}$, $4Fe^{2+}$, and $3Fe^{3+}$ has been proposed based on a comparison of average isomer shift data for FeMoco with that for an Fe^{2+} model complex with trigonal sulfur coordination.[22]

Considerably less is known about FeMoco during enzyme turnover, but states that lie either one-electron reduced or one-electron oxidized along the catalytic pathway from E_0 have been isolated and characterized. The $S = {}^3/_2$ resting state may be reduced to an EPR-silent ($S \geq 1$, most likely $S = 2$) state (M^R), which is only observed when the reduced Fe protein and MgATP are present, that is, under physiological turnover conditions.[21] For the M^N to M^R conversion, the average isomer shift (δ_{av}) remains relatively unaffected at $\Delta\delta_{av} = 0.02$ mm·s^{-1}, indicating that reduction produces only minor changes in the electron density at the Fe sites. In the absence of the reduced Fe protein and MgATP, reduction of M^N to M^R has not yet been accomplished, but an alternate one-electron reduced state (M^I) having integer electronic spin ($S \geq 1$, most likely $S = 1$) has recently been identified from radiolytic reduction of freeze-quenched M^N.[21] In contrast to the M^N to M^R conversion, δ_{av} for M^N to M^I changes by 0.05 mm·s^{-1}, suggestive that X-ray reduction occurs in the Fe portion of the cluster. The M^N state can also be observed with the addition of redox active dyes with midpoint potentials ranging 0 to -100 mV, yielding a state in which the $S = {}^3/_2$ EPR signal disappears (M^{OX}). This one-electron oxidation is fully reversible and Mössbauer[15] and MCD[16] have established that M^{OX} has a diamagnetic ground state, δ_{av} of which changes by -0.06 mm·s^{-1} relative to M^N. The inference from the changing average isomer shift values is the spin coupling pattern present in M^N no longer persists on one-electron oxidation.

Since the structural identification of FeMoco, the experimental effort to supply a detailed picture of its electronic structure and the associated nitrogen fixation process has intensified. Theoretical methods provide a complementary framework for understanding FeMoco spectroscopic and energetic features as well as insight into the structures of FeMoco intermediates prior to N_2 binding. Advances in computational chemistry,[23] principally in density functional theory (DFT),[24] have resulted in detailed electronic structure calculations on a wide variety of metalloprotein active sites.[25−32] Several quantum chemical studies at various theoretical levels have also been applied to study the electronic structure of the FeMo cofactor of nitrogenase and potential nitrogen fixation processes[33−39] (see Appendix 1).

In this work, spin-polarized density functional calculations have been used to probe several outstanding issues for the active site of nitrogenase. The distinctive feature of the calculations herein is the use of the combined spin-unrestricted and broken-symmetry wave functions to model the strong antiferromagnetic interaction in the FeMo cofactor. This approach provides a qualitatively correct electronic structure of the cluster, and reasonable estimates of the properties of the FeMo cofactor.

2. Methods

2.1. FeMo Cofactor Model. X-ray crystallographic coordinates have been reported for nitrogenase from several bacteria. They now include *Azotobacter vinelandii* (*Av*)[13,17a−c] originally refined to 2.2 Å (PDB code: 1MIN), subsequently to 2.0 Å (PDB codes: 2MIN (ox), 3MIN (red)); *Clostridium pasteurianium* (*Cp*1)[17e] to 2.0 Å (PDB code: 1MIO); and, *Klebsiella pneumoniae* (*Kp*)[17g] to 1.6 Å (PDB codes: 1QH1 (ox), 1QH8 (mixed), 1QGU (red)). Our starting geometry for the FeMo cofactor was based on the 1MIN structure. The electronic structure of several FeMo cofactor models which differ only in the ligands coordinated to Mo that approximate the endogenous organic homocitrate ligand have been examined.[40] The results here are for our largest model cluster, shown in Figure 3, which includes the $[Mo7Fe9S]^{1+}$ core, the side chain ligands of Cys275 (represented by a methyl thiolate), His442

(19) Lee, H.-I.; Hales, B. J.; Hoffman, B. M. *J. Am. Chem. Soc*. **1997**, *119*, 11395.
(20) True, A. E.; Nelson, M. J.; Venters, R. A.; Orme-Johnson, W. H.; Hoffman, B. M. *J. Am. Chem. Soc*. **1988**, *110*, 1935.
(21) Yoo, S. J.; Angove, H. C.; Papaefthymiou, V.; Burgess, B. K.; Münck, E. *J. Am. Chem. Soc*. **2000**, *122*, 4926.
(22) MacDonnell, F. M.; Rohlandt-Senge, K.; Ellison, J. J.; Holm, R. H.; Power, P. P. *Inorg. Chem*. **1995**, *34*, 1815.
(23) Siegbahn, P. E. M.; Blomberg, M. R. A. *Chem. Rev*. **2000**, *100*, 439.
(24) (a) Ziegler, T. *Chem. Rev*. **1991**, *91*, 651. (b) Ziegler, T. *Can. J. Chem*. **1995**, *73*, 743.
(25) (a) Yoshizawa, K.; Shiota, Y.; Yamabe, T. *Chem. Eur. J*. **1997**, *3*, 1160. (b) Yoshizawa, K.; Ohta, T.; Yamabe, T. *Bull. Chem. Soc. Jpn*. **1998**, *71*, 1899. (c) Yoshizawa, K. Ohta, T.; Yamabe, T.; Hoffman, R. *J. Am. Chem. Soc*. **1997**, *119*, 12311. (d) Yoshizawa, K.; Shiota, Y.; Yamabe, T. *J. Am. Chem. Soc*. **1998**, *120*, 564. (e) Yoshizawa, K.; Shiota, Y.; Yamabe, T. *Organometallics*. **1998**, *17*, 2825. (f) Yoshizawa, K. *J. Biol. Inorg. Chem*. **1998**, *3*, 318. (g) Yoshizawa, K.; Yamabe, T.; Hoffman, R. *New. J. Chem*. 1997, *21*, 151. (h) Yoshizawa, K.; Hoffman, R. *Inorg. Chem*. **1996**, *35*, 2409. (i) Siegbahn, P. E. M.; Crabtree, R. H. *J. Am. Chem. Soc*. **1997**, *119*, 3103. (j) Siegbahn, P. E. M. *Inorg. Chem*. **1999**, *38*, 2880. (k) Siegbahn, P. E. M.; Crabtree, R. H.; Nordlund, P. *J. Biol. Inorg. Chem. Soc*. **1998**, *3*, 314. (l) Basch, H.; Mogi, K.; Musaev, D. G.; Morokuma, K. *J. Am. Chem. Soc*. **1999**, *121*, 7249. (m) Dunietz, B. D.; Beachy, M. D.; Cao, Y.; Whittington, D. A.; Lippard, S. J.; Friesner, R. A. *J. Am. Chem. Soc*. **2000**, *122*, 2828.
(26) (a) Yang, Y.-S.; Baldwin, J.; Ley, B. A.; Bollinger, J. M., Jr.; Solomon, E. I. *J. Am. Chem. Soc*. **2000**, *122*, 8495. (b) Lovell, T.; Li, J.; Noodleman, L. *JBIC, J. Biol. Inorg. Chem*., submitted.
(27) Li, J.; Fisher, C. L.; Konecny, R.; Bashford, D. Noodleman, L. *Inorg. Chem*., **1999**, *38*, 929.
(28) Blomberg, M. R. A.; Siegbahn, P. E. M.; Babcock, G. T.; Wilkstrom, M. *J. Am. Chem. Soc*. **2000**, *122*, 12848.
(29) Pavlov, M.; Siegbahn, P. E. M.; Blomberg, M. R. A.; Crabtree, R. H. *J. Am. Chem. Soc*. **1998**, *120*, 548.
(30) Himo, F.; Eriksson, L. A.; Maseras, F.; Siegbahn, P. E. M. *J. Am. Chem. Soc*. **2000**, *122*, 8031.
(31) (a) Aizman, A.; Case, D. A. *J. Am. Chem. Soc*. **1982**, *104*, 3269. (b) Noodleman, L.; Case, D. A. *Adv. Inorg. Chem*. **1992**, *38*, 423. (c) Mouesca, J.-M.; Chen, J. L.; Noodleman, L.; Bashford, D.; Case, D. A.; *J. Am. Chem. Soc*. **1994**, *116*, 11898. (d) Norman, J. G., Jr.; Ryan, P. B.; Noodleman, L. *J. Am. Chem. Soc*. **1980**, *102*, 4279. (e) Noodleman, L.; Baerends, E. J. *J. Am. Chem. Soc*. **1984**, *106*, 2316. (f) Noodleman, L.; Peng, C. Y.; Case, D. A.; Mouesca, J. M. *Coord. Chem. Rev*. **1995**, *144*, 199.
(32) Blomberg, M. R. A.; Siegbahn, P. E. M.; Styring, S.; Babcock, G. T.; Åkermark, B.; Korall, P. *J. Am. Chem*. Soc. **1997**, *119*, 8285.
(33) Deng, H.; Hoffmann, R. *Angew. Chem., Int. Ed. Engl*. **1993**, *32*, 1062.
(34) (a) Stavrev, K. K.; Zerner, M. C. *Chem. Eur. J*. **1996**, *2*, 83. (b) Stavrev, K. K.; Zerner, M. C. *Theor. Chim. Acta* **1997**, *96*, 141. (c) Stavrev, K. K.; Zerner, M. C. *Int. J. Quantum Chem*. **1998**, *70*, 1159.
(35) (a) Dance, I. *Aust. J. Chem*. **1994**, *47*, 979. (b) Dance, I. *Chem. Commun*. **1997**, 165. (c) Dance, I. *Chem. Commun*. **1998**, 523. (d) Dance, I. *J. Biol. Inorg. Chem*. **1996**, *1*, 581.
(36) Siegbahn, P. E. M.; Westerberg, J.; Svensson, M.; Crabtree, R. H. *J. Phys. Chem. B*. **1998**, *102*, 1615.
(37) (a) Rod, T. H.; Hammer, B.; Nørskov, J. K. *Phys. Rev. Lett*. **1999**, *82*, 4054. (b) Rod, T. H.; Logadottir, A.; Nørskov, J. K. *J. Chem. Phys*. **2000**, *112*, 5343.
(38) Rod, T. H.; Nørskov, J. K. *J. Am. Chem. Soc*. **2000**, *122*, 12751.
(39) Szilagyi, R. K.; Musaev, D. K.; Morokuma, K. *Inorg. Chem*. **2001**, *40*, 766.

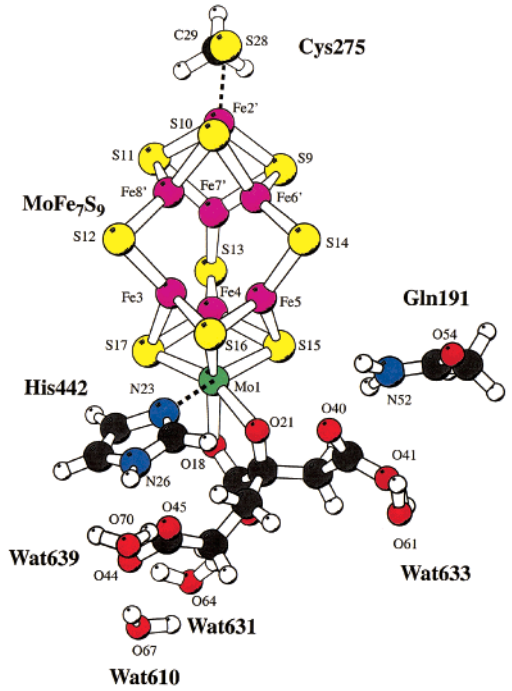

Figure 3. The FeMoco active site cluster model. Atoms are identified by color. Fe: magenta. Sulfur: yellow. Molybdenum: green. Oxygen: red. Nitrogen: blue. Carbon: dark gray. Hydrogen: white. Figure 3 was prepared using MOLSCRIPT: Kraulis, P. J. *J. Appl. Crystallogr.* **1991**, *24*, 946.

(represented by an imidazole) and the fully deprotonated homocitrate ligand (charge = −4) within the first coordination shell. A number of second shell ligands have also been included in the model: the side chain of Gln191 (represented by acetamide) and four structurally characterized water molecules (Wat639, Wat610, Wat631 and Wat633 from 2MIN) which are the hydrogen-bonding partners to the negatively charged oxygen ends of the homocitrate ligand.

2.2. Density Functional Calculations. The Amsterdam Density functional package (ADF, version 2.3)[41] was used to compute the geometries and energies of the active site clusters. The ADF basis set IV was used for all atoms, corresponding to uncontracted triple-ζ Slater-type orbitals (STO) for the 4s, 4p, 5s, and 4d valence orbitals of Mo and 3s, 3p, 4s, and 3d valence orbitals of Fe, triple-ζ STOs for the 2s, 2p valence orbitals of C, N, O augmented with a 3d polarization orbital, and triple-ζ STO for 1s of H with a 2p polarization orbital.[42,43] Electrons in orbitals up to and including 3d {Mo}, 2p {Fe, S}, and 1s {N, O, C} were considered to be part of the core and treated in accordance with the frozen core approximation. The numerical integration scheme was the polyhedron method developed by te Velde et al.[44] For all geometry optimizations, the analytical gradient method implemented by Versluis et al.[45,46] was used with a numerical integration accuracy of 4.0. Convergence criteria were set to 0.001 Å in coordinates and 0.01 Hartree/Å in the norm of all gradient vectors. The geometry optimizations in this paper were performed using the generalized gradient correction terms included in the SCF potential (local Vosko−Wilk−Nusair (VWN) + nonlocal Becke−Perdew (BP86) for exchange and correlation).[47,48]

Calculations were performed without symmetry using a parallel version of the ADF code on four SGI R10000 nodes. Within the Mo7Fe9S(Cys275·Sγ)(His442·Nδ)2O core, all bond lengths and angles were fully optimized.[49] With the exception of the atoms directly ligated to the Mo and 7Fe centers, the internal geometries (but not the relative positions) of coordinated protein residues within the first sphere, such as the imidazole ring and the methyl component of the methyl thiolate group, were constrained to their X-ray coordinates. Second shell ligands were given all degrees of freedom, allowing for the possible transfer of protons between the unsaturated oxygens of the homocitrate and the second shell hydrogen-bonding ligands (Gln191 and four waters) to occur.[49c]

To describe spin polarization and spin coupling, the calculations were done with the spin-unrestricted broken-symmetry (BS) approach.[50] The BS state is not a pure spin state, but rather a mixed state in which the majority spin and minority spin are arranged either spin-up and spin-down to give a spin coupling pattern with the correct net total spin and either an overall antiferromagnetic or ferromagnetic alignment. The energy of such a BS state is usually above, but close to, the true ground-state energy.[51] To construct a desired BS state, a calculation on the high-spin (HS) state is first completed, which is a pure spin state described by a single determinant, with all unpaired electrons aligned in the same direction (spin-up) to adopt the highest possible total spin state S. For the $Mo^{4+}6Fe^{2+}1Fe^{3+}$ oxidation state, the high-spin state has total spin $S = {}^{29}/_{2}$; for $Mo^{4+}4Fe^{2+}3Fe^{3+}$, the maximum spin is $S = {}^{31}/_{2}$. The density of the HS state is then manipulated by exchanging designated blocks of α and β electron densities. In this way, the starting density for the desired spin-flipped $S = {}^{3}/_{2}$ state is created, from which BS states are obtained by SCF convergence.[52]

Relative to the proposed resting M^N states, calculations have also been undertaken for other states of the catalytic cycle, including the spectroscopically characterized diamagnetic state M^{OX} which lies one-

(40) The three alternative models differ in the nature of the groups used to approximate the homocitrate ligand. The quantum active sites included ones in which the $CH_3CO_2^-$ and $CH_3CH_2CO_2^-$ groups of the homocitrate and its relevant hydrogen bonding partners were replaced by: (1) a dichloride model and (2) a dimethyl model or (3) a model in which the entire homocitrate, its relevant hydrogen bonding partners and His442 were replaced by three hydroxo groups. The results of our largest model containing 72 atoms are presented in this work.

(41) ADF 2.3.0, Department of Theoretical Chemistry, Free University of Amsterdam, 1997.

(42) (a) Snijders, J. G.; Baerends, E. J.; Vernooijs, P. *At. Data Nucl. Data Tables* **1982**, *26*, 483. (b) Vernooijs, P.; Snijders, J. G.; Baerends, E. J. *Slater Type Basis Functions for the Whole Periodic System*; Internal report; Free University of Amsterdam: The Netherlands, 1981.

(43) Krijn, J.; Baerends, E. J. *Fit Functions in the HFS-method*; Internal report (in Dutch); Free University of Amsterdam: The Netherland, 1984.

(44) (a) Boerrigter, P. M.; te Velde, G.; Baerends, E. J. *Int. J. Quantum Chem.* **1988**, *33*, 87. (b) te Velde, G.; Baerends, E. J. *J. Comput. Phys.* **1992**, *99*, 84.

(45) Versluis, L.; Ziegler, T *J. Chem. Phys.* **1988**, *88*, 322.

(46) Schlegel, H. B. *Ab initio Methods in Quantum Chemistry*; Lawley, K. P., Ed; Advances in Chemical Physics, Vol. 67, Part I; Wiley: New York, 1987.

(47) Vosko, S. H.; Wilk, L.; Nusair, M. *Can. J. Phys.* **1980**, *58*, 1200.

(48) (a) Perdew, J. P.; Chekavry, J. A.; Vosko, S. H.; Jackson, K. A.; Perderson, M. R.; Singh, D. J.; Fioihais, C. *Phys. Rev. B.* **1992**, *46*, 6671. (b) Becke, A. D. *J. Chem. Phys.* **1986**, *84*, 4524.

(49) (a) We have fully optimized the model in which the homocitrate and external hydrogen bonding partners have been replaced by a dimethyl moiety. The homocitrate and relevant hydrogen bonding partners were then grafted back onto the optimized geometry of the smaller dimethyl model by direct replacement of the two methyl groups for all 12 BS states. The energies were compared at the nonrelativistic single-point level. For the lowest-lying spin state alignments, BS2, BS6, and BS7, the largest quantum model was fully geometry-optimized, and the trends in both geometry and energy were compared with (1) the dimethyl model alone and (2) the large model in which the homocitrate and hydrogen bonding partners were grafted back onto the dimethyl FeMoco core geometry. The geometric and energetic parameters differ only slightly when comparing the homocitrate grafted model with both the dimethyl model and the fully optimized model. Where appropriate, we report the results for the largest model clusters that have been fully optimized, and this is indicated in the accompanying text. (b) Total spin states of $S = {}^{1}/_{2}$ and $S = {}^{5}/_{2}$ for FeMoco have also been calculated. For the few spin states examined, these states are also noted to lie low in energy. The energies associated with the many possible spin-coupling alignments satisfying these total cluster spin criteria is not covered in this work. (c) Intramolecular proton transfer from the second shell hydrogen bonding partners and the oxygen ends of the homocitrate ligand did not occur.

(50) Noodleman, L. *J. Chem. Phys.* **1981**, *74*, 5737.

(51) (a) The broken-symmetry state is not a pure spin state described by a single determinant, but rather a weighted average of pure spin states. Since the weighting factor of each pure spin state is known, from Clebsch−Gordan algebra, the broken-symmetry energy can be expressed in terms of the energies of the pure spin states. For more detail, see ref 50 and references therein. (b) Lovell, T. Ph.D. Thesis, The Australian National University, 1998. (c) McGrady, J. E.; Stranger, R.; T. Lovell, *J. Phys. Chem. A* **1997**, *101*, 6265.

electron oxidized relative to M^N, as well as the catalytically and radiolytically observed one-electron reduced species, M^R and M^I, respectively. For M^{OX}, spin states of $S = 0$, 1, and 2 were constructed, with $S = 0$ generated from $S = {}^3/_2$ by removal of one α electron followed by a single-spin transition to give a state with an equal number of α and β electrons. M^{OX} $S = 1$ has an excess of two α spin electrons and M^{OX} $S = 2$ has an excess of four α spin electrons. Similarly, M^R ($S = 2$) and M^I ($S = 1$) have excesses of four and two α spin electrons, respectively, and no spin transitions are required.

3. Results

3.1. Spin Coupling in FeMo Cofactor. The resting state of nitrogenase exhibits an $S = {}^3/_2$ EPR signal resulting from the FeMoco.[9] Using spin-projection coefficient analysis procedures developed in our laboratory,[53a,b] Lee et al.[19] have proposed an assignment of the metal-ion valencies from their ^{57}Fe Q-band ENDOR measurements. This proposal of $[Mo^{4+}Fe^{3+}6Fe^{2+}9S^{2-}]^+$ gives a formal d-electron count of 43. Even with a $S = {}^3/_2$ ground spin state and a spectroscopic assignment of the formal valencies associated with each metal ion, the pattern of spin-up or spin-down electron density at the metal sites is not unique. Assuming high-spin transition metal ions, there are many possible spin alignment patterns which satisfy $S = {}^3/_2$ and the given metal ion valencies. In accord with the lack of observable Mo hyperfine interactions,[19] molybdenum is assumed to be in the $Mo^{4+}(d^2)$ state, and low-spin in the octahedral environment of O, N, and S-based ligands. The $S = {}^3/_2$ spin state of FeMoco therefore results from the spin coupling of one ferric (Fe^{3+}, high spin d^5, $S = {}^5/_2$) and six ferrous ions (Fe^{2+}, high-spin d^6, $S = 2$). The $S = {}^3/_2$ spin condition may be satisfied by aligning the Fe site spin vectors in the following way:

$$\begin{aligned} M_s(\text{total}) &= M_s(\text{3Fe Triangle}) + M_s(\text{4Fe′ Cubane}) \\ &= M_s(\text{Fe}_3 + \text{Fe}_4 + \text{Fe}_5) + M_s(\text{Fe}_2' + \text{Fe}_6' + \text{Fe}_7' + \text{Fe}_8') \\ &= (+2 - 2 - 2) + ({}^{-5}/_2 + 2 + 2 + 2) \\ &= {}^3/_2 \end{aligned} \quad (1)$$

This is one of a number of possible spin alignments. However, all the spin alignments corresponding to the two $M_s(\text{total}) = {}^{\pm 3}/_2$ values give a 4:3 pattern, that is, 4 Fe sites of majority spin up and 3 Fe sites of majority spin down or vice versa. Neglecting the N and S connections to the protein and the O atoms of the endogenous homocitrate ligand, the cluster exhibits an approximate C_3 axis of rotational symmetry, which results in 10 possible spin alignment patterns (Figure 4). Figure 4 also shows the spin alignment for the HS state, in which all Fe site spin vectors are aligned:

$$M_s(\text{total}) = (+2 + 2 + 2) + ({}^{+5}/_2 + 2 + 2 + 2) = {}^{29}/_2 \quad (2)$$

3.2. Gas-Phase Energetics and Optimized Geometries. Table 1 shows the optimized energies of the 10 simple BS spin states,[49a] each satisfying the spin criteria of $S = {}^3/_2$,[49b] together with the energy of the HS state ($S = {}^{29}/_2$). State BS2 lies lowest in energy; however, when the effects of the protein and solvent environment are taken into account, state BS6 lies lowest in energy, as we show elsewhere.[53c] The other nine BS states are excited states ranging from 3.7 to 22.7 kcal/mol above BS2. The HS state is about 64 kcal higher in energy than BS6 at their respective optimized geometries. Such a large energy difference clearly indicates the important role played by antiferromagnetic coupling between Fe sites in the stabilization of the FeMo cofactor. Figure 5 shows an approximate correlation of stability with the number of antiferromagnetic (AF) Fe pairs, favoring BS states with an increasing number of AF interactions. Generally, BS6 and BS2 are the only spin alignments that display 3 AF interactions between Fe_2' and sites Fe_6', Fe_7' and Fe_8' and are lowest in energy, within 4 kcal/mol of each other. BS7 and all other states lie higher in energy and display fewer AF interactions involving Fe_2'. As discussed below, this is probably correlated with ferric character of Fe_2', since Fe(III)/Fe(II) AF interaction energies are generally larger than those for Fe(II)/(Fe(II) pairs.

Table 2 gives a comparison of the calculated geometric parameters for the three lowest-lying BS spin states and the HS state with crystallographic data. The optimized geometries have been least-squares fit[54a,b] to the 2.2 and 2.0 Å X-ray coordinates of the *Av* protein structure and the 1.6 Å *Kp* structure. In Figure 6, a and b, respectively, the geometry optimized structures (in black) for BS6 and BS2 are superimposed on the X-ray coordinates (in white) of the 1.6 Å *Kp* protein, and the corresponding superposition statistics are given in Table 2.

The optimized Mo−Fe, Fe−Fe, and Fe′−Fe′ bond lengths for BS6 are significantly shorter than for the 2.2 Å structure[17] that was used for our starting geometry and are a better match to the other protein data sets than are the BS2, BS7, or HS structures. The differences between the optimized BS6 parameters and their crystallographic counterparts are small (See Figure 6a and Table 2), mainly occurring for intracubane Mo−Fe, Fe−Fe, Fe′−Fe′, and Fe−S distances, with errors no greater than 0.09 Å. Slightly larger deviations are observed for Mo−S, Mo−O, Mo−N, and intercubane Fe−Fe′ distances. It is worth noting that the space across the central waist of the FeMo cofactor is smallest in the 2.2 Å structure (Fe−Fe'_{av} = 2.51 Å). In the more refined structures, Fe−Fe'_{av} increases from 2.55 Å in *Av* to 2.61 Å in *Kp*. For state BS6, Fe−Fe'_{av} = 2.75 Å, which is larger than in any of the crystal structures. Potential electrostatic effects of nearby positively charged residues such as Arg96 or Arg359 are absent from the quantum model. These may provide an electrostatic driving force necessary to shift the bridging μS^2 atoms toward the Arg side chains, leading to a decrease in the Fe−μS^2−Fe′ angles and an overall shortening of Fe−Fe'_{av}.

(52) (a) For the $Mo^{4+}4Fe^{2+}3Fe^{3+}$ oxidation state, problems were encountered associated with SCF convergence due to a band of approximately isoenergetic predominantly Fe-based energy levels that give rise to small HOMO−LUMO gaps of ~0.01 eV or less. Here SCF convergence was achieved by artificially shifting the virtual orbitals to higher energy by 0.3 Hartree. The converged BS wave function and geometry were then used as the starting point for our geometry-optimization calculations where this artificial shifting of virtual orbitals was not required. In all cases examined, the geometries and energies for the initial shifted and final unshifted calculations were identical. As a final check that the calculated electronic structure was correct and not an artifact of shifting incorrect virtual orbitals (done at the first SCF cycle and therefore very much dependent on the starting geometry), the Slater transition state method[52b−c] was used to ensure that the correct virtual orbitals were shifted to higher energy. (b) Slater, J. C. *Adv. Quantum Chem*. **1972**, *6*, 1. (c) Slater, J. C.: *Quantum Theory of Molecules and Solids*; New York: McGraw-Hill, 1974; Vol. 4.

(53) (a) Mouesca, J.-M.; Noodleman, L.; Case, D. A. *Inorg. Chem*. **1994**, *33*, 4819. (b) Mouesca, J.-M.; Noodleman, L.; Case, D. A.; Lamotte, B. *Inorg. Chem*. **1995**, *34*, 4347. (c) Lovell, T.; Li, J.; Case, D. A.; Noodleman, L. *JBIC, J. Biol. Inorg. Chem.*, submitted.

(54) (a) McRee, D. E.; Israel, M. In *Crystallographic Computing*; Bourne, E., Watenpaugh, K., Eds.; Oxford University Press: Oxford, U.K., 1998; Vol. 7. (b) The 2.0 and 1.6 Å higher resolution structures are expected to be better, but for historical reasons, we began with a starting geometry from the 2.2 Å structure. Consequently, optimized geometries have been RMSD matched against structures that encompass all three levels of resolution.

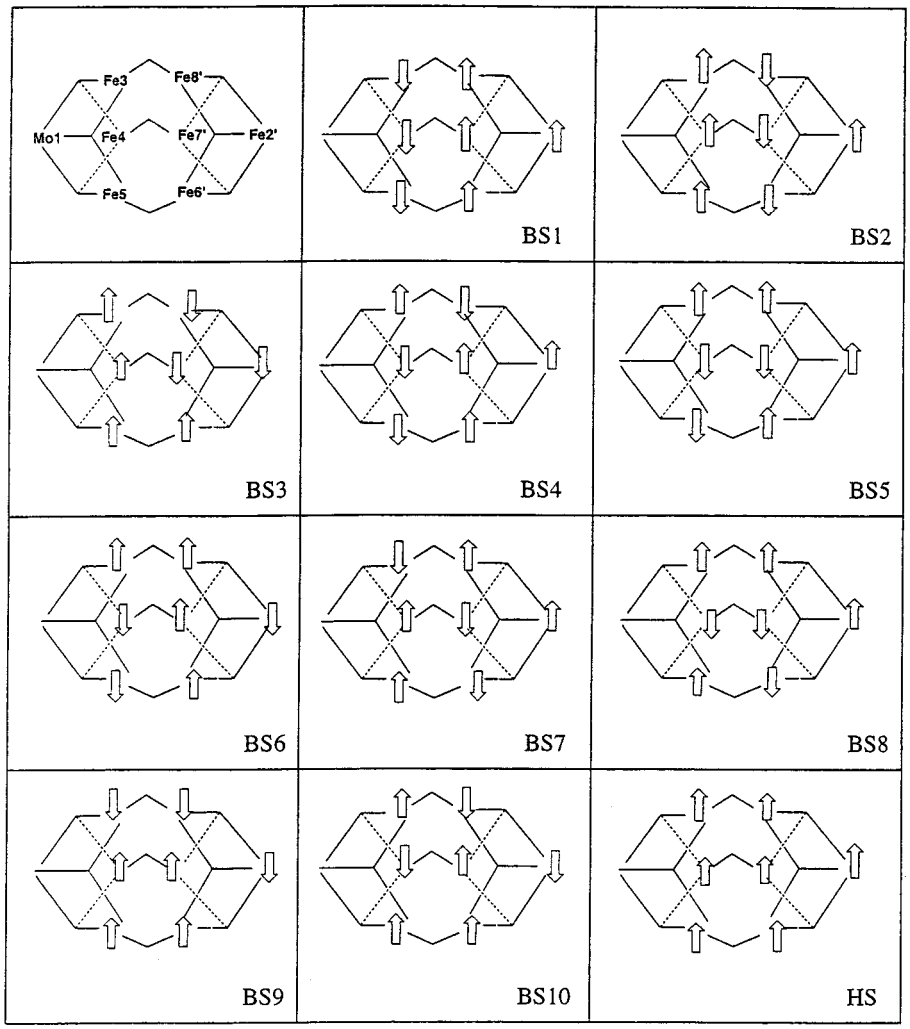

Figure 4. Spin coupling alignment for the 10 simple broken-symmetry states of the FeMoco cluster at the $Mo^{4+}6Fe^{2+}Fe^{3+}$ oxidation level.

Table 1. Optimized Energies (kcal/mol) of the 10 Simple Broken-Symmetry Spin Alignments of FeMoco at the $Mo^{4+}6Fe^{2+}Fe^{3+}$ Level[a]

state	BS1	BS2	BS3	BS4	BS5	BS6[b]	BS7	BS8	BS9	BS10	HS
rel. energy	+18.9	-3.7	+15.5	+9.3	+20.5	0.0	+2.3	+6.7	+8.2	+5.0	+63.6
AF Pair	3	6	5	8	6	7	9	7	6	8	0
F Pair	9	6	7	4	6	5	3	5	6	4	12

[a] All energies are quoted relative to BS6[b]. Also shown are the number of antiferromagnetic and ferromagnetic pairs for each spin alignment. [b] State BS6-3, see text for a detailed discussion.

Although the BS2 state is correct in having a net spin of $S = {}^3/_2$ and is lowest lying in energy in gas phase, the general size of the FeMo cofactor in this state is larger than for BS6 (Figure 6b) and this is reflected in a better agreement of BS6 with the protein geometries. The expansion of the cluster is particularly evident in the average intercubane Fe−Fe′ distances (3.25 Å) compared to BS6 (2.75 Å). The Fe−μS^2 and Fe′−μS^2 distances are almost identical to those observed for BS6 and the source of the Fe−Fe′ expansion is primarily due to the opening up of the Fe−μS^2−Fe′ angle (from Table 2, ∠Fe−μS^2−Fe′ = 96.0°). The driving force for the larger Fe−μS^2−Fe′ angle in BS2 appears to be linked to the AF spin alignment between Fe sites with bridging μS^2 atoms (Figure 4). An identical expansion (Fe−Fe′ distance large, ∠Fe−μS^2−Fe′ greater than 90°) of the cluster in this region is also observed for BS1 (geometry not shown) where a similar AF spin pattern across the central cavity exists.

Since it lacks any of the required AF interactions, the geometry of the Mo7Fe9S core in the HS state is expanded

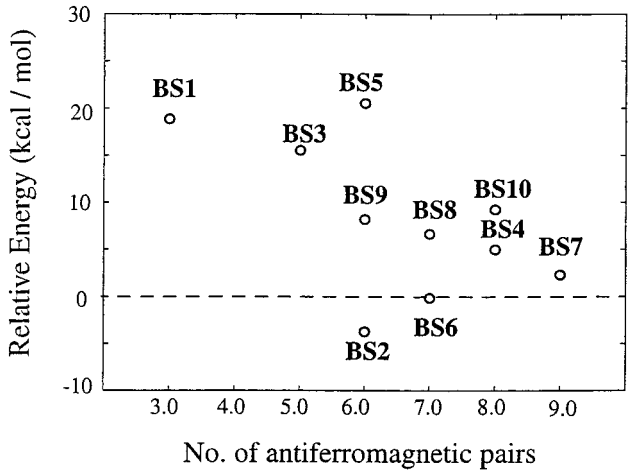

Figure 5. Gas-phase energies of the 10 simple broken-symmetry states of the FeMoco cluster at the $Mo^{4+}6Fe^{2+}Fe^{3+}$ oxidation level. All energies are plotted relative to state BS6 in kcal/mol.

Table 2. Comparison of Calculated and Experimental Geometries (Å and deg) Averaged over the Same Bond Type for $Mo^{4+}6Fe^{2+}Fe^{3+}$ FeMoco

	experiment			calculated			
				$S = {}^3/_2$		$S = {}^{29}/_2$	
	2.2 Å[b]	2.0 Å[c]	1.6 Å[d]	BS6[e]	BS7	BS2	HS
Mo−Fe	2.91	2.63	2.69	2.78	2.76	2.82	3.03
Fe−Fe	2.74	2.52	2.64	2.61	2.66	2.62	2.58
Fe−Fe′	2.51	2.55	2.61	2.75	2.74	3.25	3.28
Fe′−Fe′	2.97	2.59	2.67	2.65	2.69	2.65	2.79
Mo−O	2.24	2.02	2.32	2.14	2.14	2.13	2.12
Mo−S^3	2.46	2.24	2.34	2.42	2.42	2.42	2.44
Fe−S^2	2.12	2.17	2.21	2.20	2.20	2.19	2.24
Fe′−S^2	2.12	2.17	2.21	2.20	2.20	2.19	2.24
Fe−S^3	2.32	2.19	2.24	2.24	2.25	2.28	2.34
Fe′−S^3	2.35	2.22	2.24	2.29	2.27	2.29	2.37
Mo−N_{his}	2.25	2.13	2.47	2.29	2.30	2.31	2.30
Fe′−S_{cys}	2.29	2.32	2.32	2.30	2.31	2.30	2.33
∠Fe−μS^2−Fe′	74.3	72.0	71.5	77.6	77.0	96.0	94.1
∠Mo−μS^3−Fe	75.0	72.9	71.8	74.4	72.4	73.3	78.5
∠Fe−μS^3−Fe	78.4		71.2	71.3	72.6	71.8	72.1
RMSD fit to 2.2 Å *Av*[f]				0.37	0.43	0.54	0.68
core[g]				0.33	0.37	0.49	0.62
RMSD fit to 2.0 Å *Av*[f]				0.63	0.69	0.75	0.86
core[g]				0.33	0.36	0.47	0.59
RMSD fit to 1.6 Å *Kp*[f]				0.83	0.88	0.92	1.02
core[g]				0.31	0.35	0.44	0.55

[a] For the 10 simple BS spin alignments, only the geometries of the lowest lying states are shown. [b] PDB code: 1MIN. [c] PDB code: 3MIN(red). [d] PDB code: 1QGU(red). [e] State BS6-3, see text for a detailed discussion. [f] Fit includes His442, HCA494, and Cys275 excluding H atoms. [g] Fit includes Mo7Fe9S(Cys275·Sγ)(His442·Nδ)2O core atoms only.

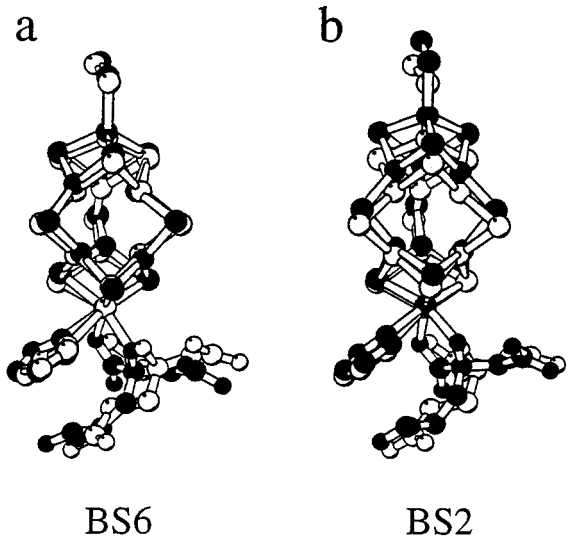

Figure 6. RMSD superposition of the optimized (black) and experimental (white) (1.6 Å *Av*) structures of the MoFe cluster for (a) BS6 and (b) BS2. Figure 6 was prepared using MOLSCRIPT: Kraulis, P. J. *J. Appl. Crystallogr.* **1991**, *24*, 946.

relative to BS2, BS6, and BS7 as well as to the active site geometry within any of the three protein data sets (see Table 2). The average intercubane Fe−Fe′ distance is 3.28 Å, notably 0.6 Å longer than the X-ray structures but similar to that in BS2. The calculated Fe′−Fe′ distances within the 4Fe′ cubane are also larger than both experiment and the BS2 or BS6 calculated parameters. In combination with the high relative energy of +64 kcal/mol (Table 1), this HS state geometry suggests that the modeling of the FeMo cofactor by a ferromagnetic high-spin state, such as in the calculations of Siegbahn et al.[36] may provide an improper representation of both the absolute geometry and energy associated with state M^N.

BS7 represents the next lowest lying BS state with spin $S = {}^3/_2$, but its higher calculated energy relative to BS6 and marginally worse heavy atom RMSDs to the experimental structures suggest this spin alignment is not as favorable as that of BS6. Nevertheless, this spin coupling alignment gives a reasonable representation of the geometry of the FeMoco core, and it is interesting to note that the geometry of BS7 falls somewhere between the geometry of BS6 and the HS state. Intercubane Fe−Fe′ distances of 2.74 Å are similar to that of BS6, while intracubane Fe′−Fe′ distances of 2.69 Å are slightly larger than those of BS6. The calculated geometries of the remaining spin coupling alignments (not shown) deviate from the experimental structures and our best calculated BS6 geometry more for all higher-lying excited states. The transition from ground (BS6) to close-lying excited states (BS2 or BS7) therefore appears to occur with only minor structural rearrangements, suggesting the geometry of the M center of nitrogenase changes only slightly on modification of the spin coupling pattern. Overall, the optimized parameters in Table 2 demonstrate the ability of the combined density functional and broken-symmetry method to model the geometry of complex polynuclear transition metal systems such as the FeMo cofactor, provided the exchange stabilization associated with the Fe sites and resultant spin coupling are treated in an appropriate manner.

3.3. Removal of the Three-Fold Degeneracy. The simple picture of the spin coupling pattern in Figure 4 is founded on the simplifying assumption that the FeMoco has an approximate three-fold axis of symmetry. However, the ligand asymmetry provided by both the homocitrate ligand and His442 residue at Mo and by Cys275 at the four-coordinate Fe site removes the three-fold symmetry axis. States BS1 and BS2 are left unchanged by cyclic permutation (∼120° rotation about the three-fold axis) of site spins within the $Fe_3Fe_4Fe_5$ spin triangle. States BS3 through to BS10, with their 2:1 pattern within the spin triangle, have three possible spin isomers, giving 26 nondegenerate BS states. Rather than examine all possible spin isomers, we focus on the three spin isomers of the low-energy state BS6 to evaluate the energetic and geometric consequences of the spin isomerization phenomenon.

Figure 7 shows the spin alignment patterns of the three "isomeric" BS6 spin states which are denoted as BS6-1, BS6-2, and BS6-3. The optimized geometries are compared with experimental structural data in Table 3. Also included in Table 3 is the accuracy of RMSD fit to experiment for each BS6 state. From the heavy atom RMSDs in Table 3 (and also Table 2) the geometry associated with any of the BS6 states is a better match to experiment than BS7, BS2, or the HS state. For states BS6-1, BS6-2, and BS6-3, all core geometries give approximately the same fit to the experimental structures, with the fit to the *Kp* protein structure better than to the *Av* structure. There is less than 1 kcal/mol energy difference in gas phase between any of the BS6 states, and thus the initial working hypothesis that assumed an approximate C_3 symmetry axis appears valid.

3.4. Fe−Fe Interactions. Since the original discovery of the geometry of the FeMo cofactor, Fe−Fe interactions playing a role in nitrogenase function have been suggested as one possible explanation for the substantial undercoordination of the three-coordinate Fe sites and overall stability of the FeMo cofactor.[55] Nearest neighbor Fe−Fe distances in metallic iron occur at 2.48

(55) Han, J.; Beck, K.; Ockwig, N.; Coucouvanis, D. *J. Am. Chem. Soc*, **1999**, *121*, 10448.

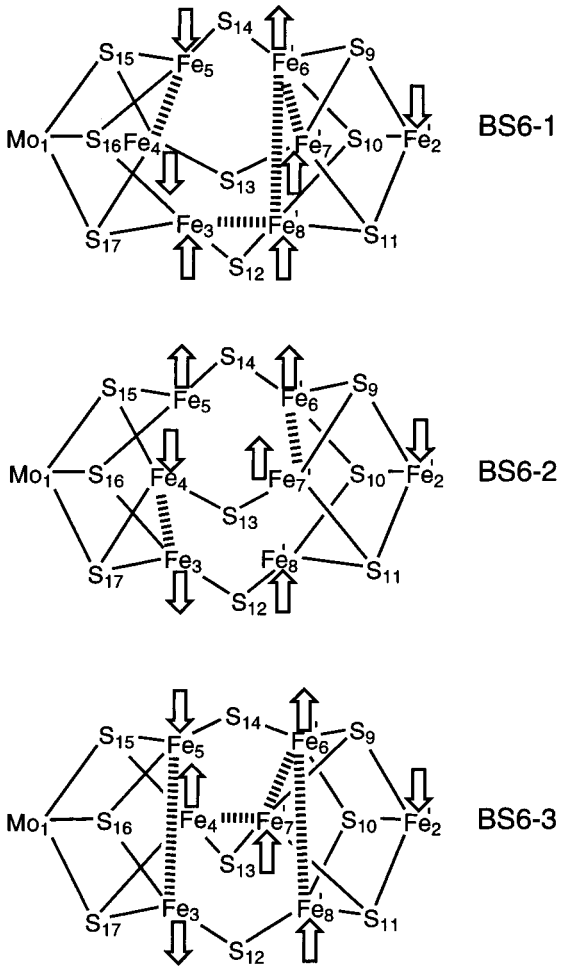

Figure 7. Spin-coupling alignment for the three spin isomer broken-symmetry states of BS6.

Å, which is commonly used as a reference when describing what constitutes an Fe−Fe bond. In Table 4, a breakdown of the calculated individual Fe−Fe, Fe−Fe′, and Fe′−Fe′ distances for the three BS6 states is presented. Short Fe−Fe interactions are indicated in bold type. The distribution of Fe−Fe interactions around FeMoco is shown as a function of the spin state isomerization within BS6 in Figure 7, with short Fe−Fe distances (Fe−Fe < 2.60 Å) indicated by a hashed line.

The shortest Fe−Fe interactions occur across pairs of Fe sites which are ferromagnetically coupled. As BS6-1 is permuted into BS6-2 and BS6-3, several short Fe−Fe interactions appear to be relatively mobile and show a significant dependency on the position of the ferromagnetic pairs of Fe sites. The possibility of this spin isomerization fluxionality being present, particularly at higher temperatures (for example, near room temperature) cannot be discounted. As one rough indicator, the HS state energy is about 64 kcal/mol above the BS6 energy. If HS is considered Fe−Fe antibonding, and BS6 is Fe−Fe bonding, then an approximate Fe−Fe bond energy can be calculated as ($^1/_2$)($^{64}/_{12}$) since there are 12 Fe−Fe nearest neighbor interactions or about 2.7 kcal/mol for each Fe−Fe bond. The fact that Fe−Fe interactions are capable of moving around the cluster in accord with the spin coupling pattern suggests that at the M^N level, Fe−Fe bonding is inherently moderately weak and the cluster does not depend on strong Fe−Fe bonding for its stability.

3.5. Orbital Energies. A simplified[56a] broken-symmetry molecular orbital energy level diagram for state BS6-1 of the FeMo cofactor is presented in Figure 8. Spin-up is the majority spin for the entire Mo7Fe spin-coupled system. The majority spin vectors representing $S = {}^5/_2$ for Fe^{3+}, $S = 2$ for Fe^{2+} associated with a particular Fe site are aligned on the figure and can be topologically mapped onto arrows and labels in Figures 3 and 7 for reference. Thus, Fe_2' is tetrahedrally coordinated; all other Fe sites are three-coordinate. The spin polarization energy associated with the presence of an excess of spin-up or spin-down electron density causes a splitting of the Fe-based 3d levels and the magnitude of the splitting reflects the net spin density on that center. For those Fe sites with majority spin-down electrons (Fe_2', Fe_4, Fe_5) all occupied low-lying Fe-based 3d energy levels are depicted as a solid band,[56b] and their higher-lying minority spin-up counterparts are shown as a dashed line.For Fe sites having majority spin-up electrons (Fe_3, Fe_6', Fe_7', Fe_8') the convention is similar (dashed band represents

Table 3. Comparison of Calculated and Experimental (Averaged over the Same Bond Type for $Mo^{4+}6Fe^{2+}Fe^{3+}$ FeMoco) Geometries (Å and deg) for the Three Isomeric Spin States of BS6[a]

	experiment		calculated $S = {}^3/_2$ spin state		
	2.0 Å[b]	1.6 Å[c]	BS6-1	BS6-2	BS6-3
Mo−Fe	2.63	2.69	2.75	2.78	2.78
Fe−Fe	2.52	2.64	2.70	2.70	2.61
Fe−Fe′	2.55	2.61	2.75	2.82	2.75
Fe′−Fe′	2.59	2.67	2.70	2.69	2.65
Mo−O	2.02	2.32	2.12	2.12	2.14
Mo−S^3	2.24	2.34	2.42	2.42	2.42
Fe−S^2	2.46	2.21	2.19	2.19	2.20
Fe′−S^2	2.46	2.21	2.19	2.19	2.20
Fe−S^3	2.32	2.24	2.23	2.24	2.24
Fe′−S^3	2.35	2.24	2.29	2.29	2.29
Mo−N_{his}	2.13	2.47	2.29	2.31	2.31
Fe'_2−S_{cys}	2.32	2.32	2.30	2.30	2.30
∠Fe−μS^2−Fe	72.0	71.5	77.6	79.6	77.6
∠Mo−μS^2−Fe	72.9	71.8	74.5	72.6	74.4
∠Fe−μS^3−Fe	71.2	71.3	71.0	74.0	72.6
RMSD to 2.2 Å *Av*[d]			0.40	0.35	0.37
core[e]			0.33	0.31	0.30
RMSD to 2.0 Å *Av*[d]			0.68	0.64	0.63
core[e]			0.33	0.30	0.30
RMSD to 1.6 Å *Kp*[d]			0.87	0.83	0.83
core[e]			0.31	0.27	0.26
relative energy (kcal/mol)			−0.16	+0.38	0.00

[a] Energies are given relative to state BS6-3 in kcal/mol. [b] PDB code: 3MIN(red). [c] PDB code: 1QGU(red). [d] Fit includes His442, HCA494, and Cys275 excluding H atoms. [e] Fit includes Mo7Fe9S(Cys275·Sγ)-(His442·Nδ)2O core atoms only.

Table 4. Comparison of Calculated and Experimental Fe−Fe Distances (Å) for $Mo^{4+}6Fe^{2+}Fe^{3+}$ FeMoco[a]

	experiment			calculated			Fe−Fe source
	2.2 Å[b]	2.0 Å[c]	1.6 Å[d]	BS6-1	BS6-2	BS6-3	
Fe_3−Fe_4	2.82	2.57	2.65	2.67	**2.56**	2.74	intracubane
Fe_4−Fe_5	2.67	2.45	2.62	**2.55**	2.79	2.74	Mo3Fe
Fe_3−Fe_5	2.72	2.53	2.66	2.62	2.74	**2.56**	
Fe_3−Fe'_8	2.51	2.60	2.62	**2.54**	2.78	2.86	intercubane
Fe_4−Fe'_7	2.61	2.57	2.62	2.90	2.89	**2.59**	Mo3Fe−4Fe′
Fe_5−Fe'_6	2.42	2.48	2.60	2.80	2.78	2.83	
Fe'_2−Fe'_6	2.99	2.64	2.66	2.76	2.75	2.76	intracubane
Fe'_2−Fe'_7	2.93	2.54	2.64	2.67	2.68	2.69	4Fe′
Fe'_2−Fe'_8	3.01	2.58	2.64	2.67	2.64	2.66	
Fe'_6−Fe'_7	2.88	2.58	2.69	**2.58**	**2.58**	**2.57**	
Fe'_7−Fe'_8	2.99	2.58	2.68	2.68	2.63	2.76	
Fe'_6−Fe'_8	3.00	2.59	2.69	**2.56**	2.63	**2.58**	

[a] Short Fe−Fe distances are in bold (see text for a detailed discussion). [b] PDB code: 1MIN. [c] PDB code: 3MIN(red). [d] PDB code: 1QGU(red).

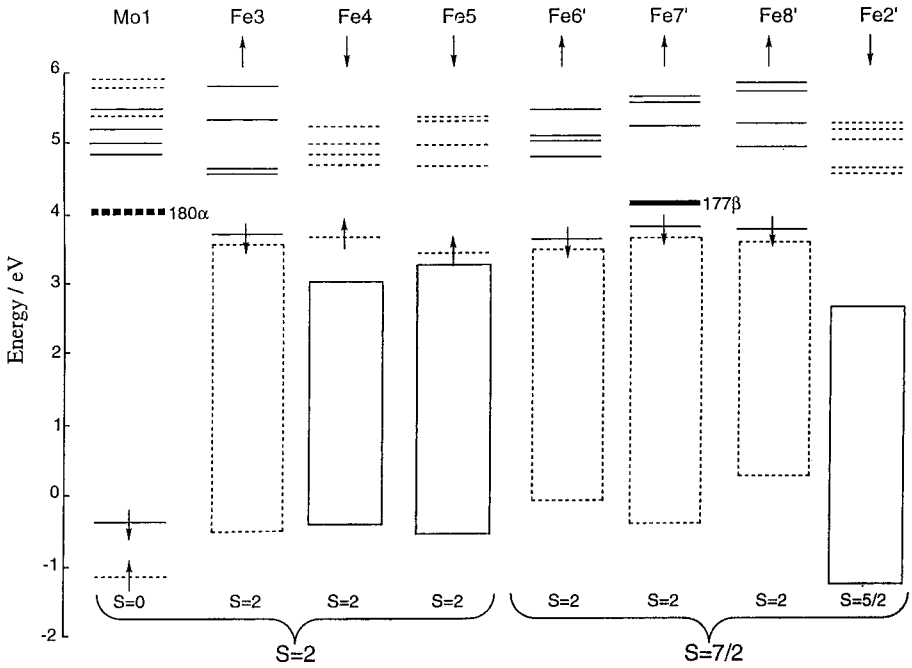

Figure 8. Energy level diagram for state BS6-1 of the FeMoco cluster at the $Mo^{4+}6Fe^{2+}Fe^{3+}$ oxidation level. A detailed description is given in the text.

spin-up energy levels, solid lines depict spin-down levels). In both cases, the highest lying occupied levels are indicated by up or down arrows in the energy level diagram. Spin polarization effects are mostly absent from the energy levels of Mo^{4+} with a d^2 ($S = 0$) configuration and a more conventional mixing of spin-up (dashed lines) and spin-down (solid lines) character in the ordering of these energy levels reflects this feature. The LUMOs of the system comprise two spatially and spin distinct components: spin-up (180↑) centered around Mo and the homocitrate ligand, and spin-down (177↓) located around the six three-coordinate Fe sites that comprise the central body of the cluster. The former lies slightly lower in energy and is indicated in bold as a dashed line while the latter is represented as a bold solid line. All energy levels below 180↑ are occupied.

From Figure 3, the strong ligand field effects of N and O in addition to S combined with the overall octahedral coordination suggest that Mo^{4+} (d^2) should adopt a low-spin configuration. The lack of any observable hyperfine coupling to Mo^{4+} in the ENDOR data also suggests that the Mo site has close to zero spin, that is, $S = 0$. The small spin density is in part a consequence of the high covalence and strong ligand field associated with the $Mo^{4+}-O$ and $Mo^{4+}-N$ bonds. Figure 8 shows that Mo has two spatially different and energetically distinct low-lying orbitals each within the t_{2g} manifold that are singly occupied with antiparallel spins.

In the presence of similar ligand fields, the magnitude of the spin polarization splitting[56c] between majority spin occupied (measured from the highest occupied molecular orbital, HOMO) and minority spin unoccupied (LUMO) energy levels should be maximal for Fe^{3+} sites. Of the Fe sites, the tetrahedrally coordinated Fe_2' exhibits the largest energetic splitting, consistent with the presence of maximum spin density at this site. In terms of formal oxidation states and coordination numbers, this would be equivalent to high-spin d^5 configuration associated with four-coordinate Fe_2', and the ligand field $e-t_2$ splitting pattern is evident in the minority spin−orbitals for site Fe_2'.

The introduction of a sixth d electron of minority spin to the remaining Fe sites (indicated by the up and down minority spin arrows in Figure 8) has several effects, including a uniform upward shift in energy of the remaining orbital energies and a reduction in the spin polarization splittings.[56d] Such qualitative features are evident in Figure 8 in the levels associated with sites Fe_3, Fe_4, Fe_5, Fe_6', Fe_7' and Fe_8' which have an occupied minority spin level above the filled majority spin levels and these sites appear to contain more ferrous character. In addition, their unusual coordination environments[57] result in substantial deviation from the typical $e-t_2$ splitting pattern within the unoccupied energy levels. From the energy levels in Figure 8, an approximate a_1-, e-, e-type (assuming C_{3v} point group) splitting pattern is observed for each of the three-coordinate Fe sites, but the degeneracy associated with the e-type manifolds is lifted. Finally, one minority spin d orbital per ferrous site is occupied and lies stabilized in energy relative to its four unoccupied counterparts. The remaining 29 Fe-based d orbitals lie close to the Fermi level (within about 2 eV) and constitute

(56) (a) The pure ligand-based levels (S, O, N, C) have been excluded from the plot for both simplicity and clarity. (b) Identification of specific occupied Fe^{2+} and Fe^{3+} 3d levels presents a problem. Extensive Fe−S covalency is apparent in the Fe 3d levels, evident from the total metal and ligand contributions. The combined effect of covalency plus a large spin polarization splitting makes the exact isolation of the occupied Fe^{2+} and Fe^{3+} 3d levels difficult as the Fe 3d character is spread over a wide range of energies in each of the occupied orbital sets. In Figure 8, the occupied Fe 3d levels are thus represented by the extended band of low-lying levels spread over a 4−5 eV range. Solid and dashed lines represent spin-up (↑) and spin-down (↓) character of an individual energy level within a band, respectively. (c) The magnitude of the spin polarization splitting between up and down spin orbitals on the same center can be traced to the single ion-exchange energy, which is greatest for high-spin d^5 systems and the defining principles of which are manifested in Hund's rule. For simplicity, the magnitude of the spin polarization energy is, to a first approximation, proportional to the number of pairwise interactions between electrons of like spin, i.e., SPE $\propto n(n-1)/2$ where $n =$ the number of unpaired electrons on that center. (d) Lovell, T.; Stranger, R.; McGrady, J. E. *Inorg. Chem.* **2001**, *40*, 39.

(57) Although the Fe sites surrounding the central cavity appear three-coordinate, and therefore substantially undercoordinated, weaker through-space interactions with other Fe sites in close proximity may fill the remaining vacancies in the coordination sphere of each Fe and give rise to higher coordination environments than would have been anticipated on the basis of through-bond interactions with S-based ligands alone.

a band of unoccupied orbitals into which electrons could be readily deposited.[58] It is worth noting the second LUMO (177↓) is centered around the orbitals of the three-coordinate Fe sites and lies only 0.11 eV higher in energy than the Mo-based LUMO (180↑) of opposite spin.

Subsequent (more reduced) states of the FeMo cofactor during enzyme turnover provide clues about the electronic structure at the M^N level. The $S = {}^3/_2$ resting state has been shown to be reducible to: (1) an EPR-silent ($S \geq 1$, probably $S = 2$) state (M^R) observed under physiological turnover conditions and (2) a different one-electron reduced state (M^I) observed upon radiolytic reduction, also having integer electronic spin ($S \geq 1$, probably $S = 1$). These total system spins, $S = 2$ for M^R and $S = 1$ for M^I, are the same as those resulting from filling the Mo-based 180↑ LUMO and the Fe-based 177↓ LUMO, respectively, and are consistent with those postulated from recent Mössbauer isomer shift and hyperfine analyses.[21] For the M^N to M^R conversion, a largely unaffected average isomer shift indicates that reduction is not primarily centered on or around the Fe sites. This is in contrast to M^I, where a notable alteration in the average isomer shift is observed, suggesting that the reduction is centered on Fe-based orbitals. Isovalue surface plots of the two LUMOs (180↑ and 177↓) are given in Figure 9. In each plot, the major contributing atomic components to the molecular orbital are indicated schematically below each isosurface plot for the relevant portion of the FeMo cofactor. Both orbitals are delocalized over several atoms, but 180↑ displays a substantial Mo component and 177↓ has only Fe character. The reduction of FeMoco by a single electron would therefore place the additional electron into orbitals having primarily Mo or Fe character. If reduction were centered on Mo, the total spin of the FeMo cofactor would increase to $S = {}^3/_2 + {}^1/_2 = 2$; if the reduction were to take place on the Fe sites, the total spin of the FeMo cofactor would decrease to $S = {}^3/_2 - {}^1/_2 = 1$. For both of these one-electron reduced states, the resultant total spin associated the FeMo cofactor would be consistent with the $S \geq 1$ expectations from the modified Lowe−Thorneley scheme (Figure 2).[14]

The relative energies and composition of each energy level within FeMoco are noted to vary as a function of the alignment of electron spins within each of the BS6 manifolds; as site spin vectors are permuted, the energy level ordering within BS6-1 becomes notably different to BS6-2 and BS6-3. Additional variation in energy level ordering occurs within the other nine BS states. Of the 12 BS states examined, BS6-1 is the only spin alignment pattern displaying an electronic structure that rationalizes the Mössbauer observations noted previously, that is, a spin-up LUMO displaying a significant Mo-based component. All other alignment patterns give rise to LUMOs whose majority spin components involve three-coordinate Fe sites around the central cavity.

3.6. Fe 3d and Spin Populations. Mulliken spin populations provide an additional measure of ligand covalency and oxidation state. Table 5 shows a Mulliken spin density analysis for state BS6-1. The calculated spin densities are compared to: (1) ideal spin populations generated for an FeMo cofactor in which Fe_2' is assigned formally as the ferric site and bonding is of a purely ionic nature; (2) spin densities of analogous Fe_4S_4 clusters. For clarity, the calculated d spin densities are further broken down into the ↑ and ↓ d populations, the total (↑+↓) and net (↑−↓) spin

(58) There are several close lying and readily available orbitals into which electrons may be easily deposited. This *band type* of electronic structure is a common feature amongst metal-based and semiconducting materials and the electronic structure of the nitrogenase FeMo cofactor appears to be quite similar in this respect.

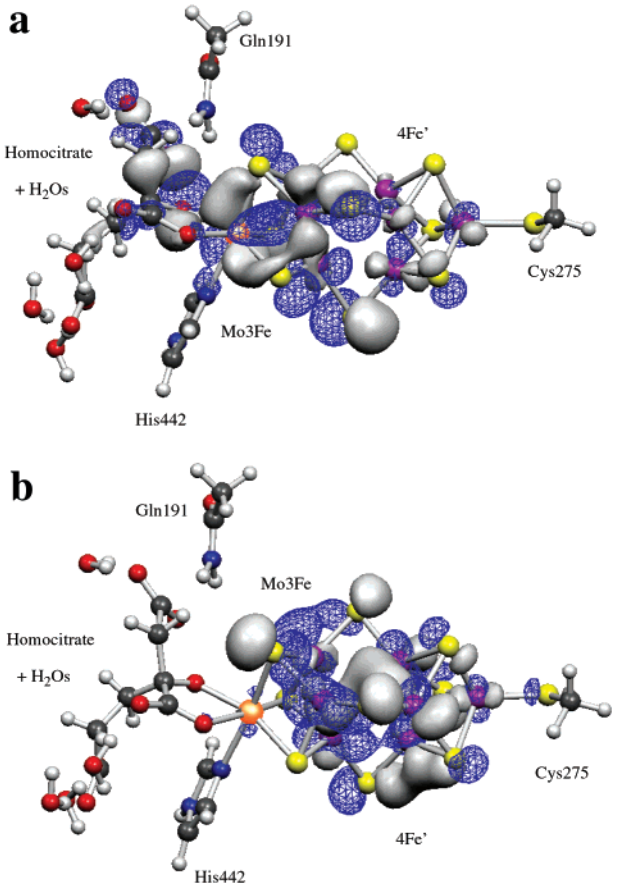

Figure 9. Isosurface contour plots of (a) spin-up (180↑) and (b) spin-down (177↓) components of the LUMO for state BS6-1 of the FeMoco cluster at the $6Fe^{2+}Fe^{3+}$ oxidation level. Atoms are identified by color. Fe: magenta. Sulfur: yellow. Molybdenum: orange. Oxygen: red. Nitrogen: blue. Carbon: dark gray. Hydrogen: light gray. Figure 9a and b was produced using *Molekel 4.1*, Flükiger, P.; Lüthi, H. P.; Portman, S; Weber, J. Swiss Center for Scientific Computing: Manno (Switzerland), 2000−2001.

populations (the final overall spin density). The net spin population includes minor s and p contributions in addition to the much larger d contributions. For comparison with Table 5, the net spin densities associated with the other low lying BS states, BS6-2, BS6-3, BS2, and BS7 are given in Table 6 for the metal-based and sulfur-based ligands of the FeMoco core.

Table 5 shows values that are much less than those expected based on the formal oxidation states and electron counts. From a purely ionic perspective, ferric sites should have five majority unpaired electrons while ferrous sites have four electrons of majority spin. Net spin densities of much less than either five or four suggests a significant amount of spin density must be lost due to metal−ligand covalency or metal−metal interaction effects. Sites Fe_2' and Fe_6' display the largest resultant net spin of 3.01. From eq 1, the Fe^{3+} site must have its d spin vector opposite to the net system spin, consistent only with the assignment of Fe_2' (−3.01) and not Fe_6' (+3.01) as the "ferric" site. Coupled with the spin polarization effects imposed on the one-electron energy levels (Figure 8) and the high-spin density associated with site Fe_2', a ferric assignment is indicated for Fe_2'. Calculated net spin densities for the remaining Fe sites are lower than 3.01, consistent with the presence of less unpaired net spin density.

From Table 5 the ideal net spin density for the Mo site is expected to be zero. For state BS6-1, the Mo spin density is calculated to be low, consistent with the absence of any observed

Table 5. Calculated Spin-Up (↑), Spin-Down (↓), Total (↑ + ↓) Fe 3d Spin Populations and Net Spin Populations[b] for $Mo^{4+}6Fe^{2+}Fe^{3+}$ FeMoco State BS6-1[a]

	FeMoco cluster								Fe_4S_4 cluster				
	ideal				calculated				calculated				
	(↑)	(↓)	(↑ + ↓)	net[b]	(↑)	(↓)	(↑ + ↓)	net[b]		(↑)	(↓)	(↑ + ↓)	net[b]
									Ferredoxin[c]				
Mo1	1	1	2	0	2.09	2.04	4.13	0.03	Fe1	1.82	4.75	6.57	3.13
Fe2	0	5	5	5	1.85	4.73	6.58	−3.01	Fe2	1.82	4.75	6.57	3.13
Fe3	5	1	6	4	4.59	2.04	6.63	2.66	Fe3	4.75	1.82	6.57	−3.13
Fe4	1	5	6	4	2.00	4.63	6.63	−2.70	Fe4	4.75	1.82	6.57	−3.13
Fe5	1	5	6	4	2.16	4.52	6.68	−2.40					
Fe6	5	1	6	4	4.67	1.83	6.50	3.01					
Fe7	5	1	6	4	4.64	1.88	6.52	2.97					
Fe8	5	1	6	4	4.63	1.93	6.76	2.67					
									Reduced Ferredoxin[d]				
									Fe1	1.75	4.79	6.54	−3.23
									Fe2	4.82	1.74	6.56	3.23
									Fe3	4.83	1.74	6.57	3.25
									Fe4	4.82	1.76	6.58	3.19
									All Ferrous[e]				
									Fe1	1.85	4.75	6.60	−3.10
									Fe2	4.88	1.68	6.56	3.35
									Fe3	4.89	1.67	6.56	3.36
									Fe4	4.89	1.68	6.56	3.36

[a] Values are compared to a ferredoxin $[Fe_4S_4(SR)_4]^{2-}$, reduced ferredoxin $[Fe_4S_4(SR)_4]^{3-}$ and all-ferrous $[Fe_4S_4(SR)_4]^{4-}$ clusters. [b] Net (↑ − ↓) spin populations include s + p + d contributions. [c] Optimized $[Fe_4S_4(SR)_4]^{2-}$ cluster ($S = 0$) in C_{2v} broken symmetry.[60] [d] Optimized $[Fe_4S_4(SR)_4]^{3-}$ cluster ($S = {}^7/_2$) in C_{2v} broken symmetry.[60] [e] Optimized $[Fe_4S_4(SR)_4]^{4-}$ cluster ($S = 4$) with no symmetry constraints.[60]

Table 6. Calculated Mulliken Net Spin Populations for the $Mo^{4+}6Fe^{2+}Fe^{3+}$ FeMoco Cluster[a]

state	Mo_1	Fe_2	Fe_3	Fe_4	Fe_5	Fe_6	Fe_7	Fe_8
BS6-1	0.03	−3.01	2.66	−2.70	−2.40	3.01	2.97	2.67
BS6-2	0.16	−3.01	−2.81	−2.89	2.77	2.95	2.96	2.84
BS6-3	0.16	−3.01	−2.73	2.77	−2.59	3.01	2.76	2.91
BS2	−0.65	3.07	3.01	3.09	2.94	−3.01	−3.03	−2.96
BS7	−0.34	2.94	−2.77	2.86	2.70	−2.81	−2.81	2.94

	S_9	S_{10}	S_{11}	S_{12}	S_{13}	S_{14}	S_{15}	S_{16}	S_{17}	S_{28}
BS6-1	0.04	0.00	0.03	0.28	−0.02	−0.02	−0.07	−0.00	−0.03	−0.14
BS6-2	0.05	−0.01	0.03	0.04	0.02	0.30	0.01	0.02	−0.12	−0.13
BS6-3	0.04	−0.00	0.02	0.02	0.20	−0.02	−0.01	−0.07	0.01	−0.14
BS2	−0.02	0.03	−0.02	−0.04	−0.03	−0.01	0.19	0.12	0.21	0.14
BS7	−0.05	0.05	0.07	0.05	−0.04	0.00	0.12	0.01	0.04	0.12

[a] Positive spin populations correspond to an excess of α-spin at those centers.

Mo ENDOR hyperfine signals.[19] In fact, from Table 6, calculated Mo spin densities are generally close to zero for all of the BS6 states, with state BS6-1, the BS6 state with a qualitatively correct electronic structure, notably the lowest. The Mo spin density is observed to increase for states BS7 and BS2, a consequence of the reorientation of several majority spin vectors, some of which are associated with Fe sites of the Mo3Fe cubane. More variation in the spin density is noted for the Mo^{4+} site across the 5 BS states in Table 6 compared to the spin densities of the Fe sites.

The calculated spin densities of FeMoco may also be compared to typical iron−sulfur clusters.[60] Spin densities are reported in Table 5 for $Fe_4S_4(SCH_3)_4^{2-}$ ($S = 0$), one-electron reduced ferredoxin ($S = {}^7/_2$) and the two-electron reduced ferredoxin (all-ferrous cluster, $S = 4$). $S = {}^7/_2$ was chosen as the reduced 4Fe ferredoxin rather than the usually observed $S = {}^1/_2$ form because $S = {}^7/_2$ resembles the 4Fe′ cubane part of state BS6. Regardless of which Fe_4S_4 cluster the comparison is made to, the spin densities within FeMoco are generally much lower than those calculated for the simple cubanes. The average Fe−S distance in FeMoco is typically shorter than even in the all-ferrous Fe_4S_4 cubane by 0.08 Å[17i] (comparing the 4Fe′ cubane of FeMoco) and 0.13 Å (Mo3Fe cubane of FeMoco) and Fe−Fe distances are similarly shorter on average. Both factors favor enhanced metal−ligand and metal−metal bond formation and reduce the spin density associated with any of the Fe sites, especially for the six three-coordinate sites. To maintain the unique structure, an enhanced degree of electron delocalization appears a requirement for FeMoco stability. In this respect, the larger, catalytic FeMoco differs from the smaller electron-transfer ferredoxins.

For the bridging μS^2 atoms, the location of the spin density per sulfide atom varies according to the ferromagnetic versus antiferromagnetic alignment of electron spins (the spin density is larger for the ferromagnetic alignment of the bonded Fe sites). The spin density associated with the μS^3 sulfide atoms (on the 4Fe′ cubane particularly) remains fairly insensitive to the spin coupling mode employed. Nevertheless, for both μS^2 and μS^3 sulfide atoms, atomic p orbital spin populations (not shown) reveal the origin of the spin density associated with the S

(59) Fe = 3d; Mo = 4d.

(60) (a) Torres, R. A.; Lovell, T.; Noodleman, L.; Case, D. A. Manuscript in preparation. (b) Liu, T.; Noodleman, L.; Case, D. A. Manuscript in preparation.

Table 7. Comparison of Calculated[a] and Observed Hyperfine A Coupling Parameters (^{57}Fe) in Nitrogenase (MHz)

	$\|\,^3/_2; {}^7/_2\ 6\ 4; 2\ 4\rangle$			$\|\,^3/_2; {}^7/_2\ 6\ 4; 2\ 3\rangle$			$\|\,^3/_2; {}^7/_2\ 5\ 4; 2\ 3\rangle$				
	A_{calc}			A_{calc} (canted)			A_{calc} (canted)				
site	BS6-1	BS6-2	BS6-3	BS6-1	BS6-2	BS6-3	BS6-1	BS6-2	BS6-3	A_{exp}	site type
B^1	+14.7	+15.1	+14.8	+8.8	+9.1	+8.9	+8.8	+9.1	+8.9	+11.7	Fe^{2+} triangle
B^2	+13.2	+15.6	+14.8	+7.9	+9.4	+8.9	+7.9	+9.4	+8.9	+9.3	Fe^{2+} triangle
A^4	−11.4	−12.0	−11.4	0.0	0.0	0.0	0.0	0.0	0.0	−3.7	Fe^{2+} triangle
A^1	−23.1	−22.8	−23.0	−23.0	−22.8	−23.0	−19.2	−18.9	−19.1	−18.0	Fe^{2+} cubane
A^2	−22.5	−22.5	−21.1	−22.4	−22.5	−21.1	−18.6	−18.6	−17.5	−17.1	Fe^{2+} cubane
A^3	−20.5	−21.6	−22.1	−20.5	−21.6	−22.1	−12.4	−13.0	−13.3	−11.8	Fe^{2+} cubane
B^1	+17.5	+17.5	+17.5	+17.5	+17.4	+17.5	+5.5	+5.5	+5.5	+11.7	Fe^{3+} cubane

[a] $Mo^{4+}6Fe^{2+}Fe^{3+}$ FeMoco cluster, spin state is $|S_t; S_b\ S_{456}\ S_{45}; S_a\ S_{12}\rangle$ (see text for a description of terms).

Table 8. Comparison of Calculated[a] and Observed Hyperfine A Coupling Parameters (^{57}Fe) in Nitrogenase (MHz)

	A_{calc} BS2							A_{calc} BS7					
	1[b]	2[c]	3[d]	4[e]	expt.	site		1[f]	2[g]	3[h]	4[i]	expt.[j]	site
Fe3	−23.1	−23.1	−21.8	−21.8	−17.1	A^2	Fe4	−23.2	−13.9	−23.2	−13.9	−18.0	A^1
Fe4	−23.9	−23.9	−22.5	−22.5	−18.0	A^1	Fe5	−21.9	−13.2	−21.9	−13.2	−17.1	A^2
Fe5	−22.6	−22.6	−15.5	−15.5	−11.8	A^3	Fe3	+17.5	0.0	+17.5	0.0	+11.7	B^1
Fe6	+16.9	+12.5	+12.8	+9.7	+11.7	B^1	Fe2	−5.2	−5.2	−3.1	−3.1	−11.8	A^3
Fe7	+17.0	+12.6	+12.9	+9.7	+11.7	B^1	Fe8	−5.2	−5.2	−3.1	−3.1	−3.7	A^4
Fe2	−13.0	0.0	−9.4	0.0	−3.7	A^4	Fe6	+5.9	+5.9	+3.9	+3.9	+11.7	B^1
Fe8	+16.7	+12.4	+12.6	+9.5	+9.3	B^2	Fe7	+5.9	+5.9	+3.9	+3.9	+9.3	B^2

[a] $Mo^{4+}6Fe^{2+}Fe^{3+}$ FeMoco cluster, see Figure 3. Spin states $|S_t; S_b\ S_{456}\ S_{45}; S_a\ S_{12}\rangle$ are shown for BS2 and BS7 (see text for a description of terms). [b] Spin state $|^3/_2; {}^9/_2\ 2\ 4; 6\ 4\rangle$. [c] Spin state $|^3/_2; {}^9/_2\ 2\ 3; 6\ 4\rangle$ (canted). [d] Spin state $|^3/_2; {}^7/_2\ 2\ 4; 5\ 4\rangle$ (canted). [e] Spin state $|^3/_2; {}^7/_2\ 2\ 3; 5\ 3\rangle$ (canted). [f] Spin state $|^3/_2; {}^1/_2\ 2\ 4; 2\ 4\rangle$. [g] Spin state $|^3/_2; {}^1/_2\ 2\ 4; 2\ 3\rangle$ (canted). [h] Spin state $|^3/_2; {}^1/_2\ 2\ 3; 2\ 4\rangle$ (canted). [i] Spin state $|^3/_2; {}^1/_2\ 2\ 3; 2\ 3\rangle$ (canted). [j] Reference 21.

atoms: significant spin delocalization from the S-based p orbitals into the Fe based d orbitals of minority spin.

3.7. Analysis of Iron Hyperfine Data. A detailed description of the approach used to calculate the hyperfine A_{iso} values from our density functional calculations is given in Appendix 2. Initial Mössbauer studies[15] of both *Av*1 and *Cp*1 FeMo cofactors revealed at least six Fe sites grouped into two classes according to the sign of the isotropic magnetic hyperfine coupling constants (A_{iso}). The observed hyperfine parameters A_{iso} are a measure of the electronic spin density at the Fe nuclei, projected onto the total spin of the system. For FeMoco, three sites have $A_{iso} < 0$ (A^1, A^2, and A^3) while three other sites have $A_{iso} > 0$ ($2B^1$ and B^2) indicating a 3(↑):3(↓) pattern. Using isotopic hybrids of the MoFe protein, A-tensor components of the seventh site (not seen in previous Mössbauer and ENDOR analyses) have recently been identified.[21] They are found to be much smaller than those of the other Fe sites and suggest the local spin of the seventh site is oriented nearly perpendicular to the direction of the total spin (similar to that observed in 3Fe4S clusters).[21,61a,b] The hyperfine tensor associated with the seventh site is assigned as type A^4, resulting in a 4(↑):3(↓) pattern of site spins, consistent with the BS6 state from our calculations (also consistent with states BS3 through to BS10 but the majority are discounted on energetic grounds from Figure 5). On the basis of the energies in Figure 5, the spin projection analysis is only undertaken for states BS2, BS7, and the three isomers of BS6.

Table 7 compares calculated and observed hyperfine coupling parameters (^{57}Fe) for *Av*1 nitrogenase (MHz) at 4.2 K. A_{iso} values are calculated for all three BS6 states using the spin populations of the 3d orbitals for each Fe site and the spin-projection procedures detailed in Appendix 2. The explicit spin vector notation used is $|S_t; S_b\ S_{456}\ S_{45}; S_a\ S_{12}\rangle$ (see Figure 10 for visualization). The Fe triangle ($Fe_3Fe_4Fe_5$) comprises sites 1, 2, and 3 (component spins S_1, S_2, and S_3) giving a total internal spin vector $S_a = S_{123}$ and an intermediate spin vector S_{12}. The Fe cubane has its total internal spin $S_b = S_{4567}$ composed of prismane-type spin sites $S_4S_5S_6$ ($Fe_6'Fe_7'Fe_8'$) and the terminal corner site S_7 (Fe_2'). The total cluster spin $S_t = {}^3/_2$ results from the Fe_3 triangle of spin $S_a = 2$ strongly antiferromagnetically coupled to an 4Fe′ cubane of spin $S_b = {}^7/_2$. The spin state $|^3/_2; {}^7/_2\ 6\ 4; 2\ 4\rangle$ is the pure spin state which most closely resembles the broken-symmetry state BS6 in its spin coupling pattern. This spin state has calculated A_{iso} values that have a correct qualitative pattern but which are generally too large in magnitude, particularly for those sites with negative A_{iso} values. Further, the calculated magnitude of the isotropic hyperfine coupling constant for the seventh site is much larger than observed.

The calculated A_{iso} values are improved dramatically by canting (or rotating) the site spin vectors from purely parallel or antiparallel alignment. Canting of spins (shown in bold type) in the Fe_3 triangle in the spin state $|^3/_2; {}^7/_2\ 6\ 4; \mathbf{2\ 3}\rangle$ gives better quantitative agreement than $|^3/_2; {}^7/_2\ 6\ 4; 2\ 4\rangle$. Further significant improvement is associated with rotation of spin vectors within the 4Fe′ cubane and Fe_3 triangle subunits, giving an overall spin state of $|^3/_2; {}^7/_2\ \mathbf{5\ 4}; \mathbf{2\ 3}\rangle$. This canting of spins in the FeMo cofactor affords a good quantitative agreement between the experimental data and our calculated isotropic hyperfine coupling constants, with the largest deviation of about 6 MHz observed for the B^1 Fe^{3+} site of the cubane. Most significantly, the magnitude of the A_{iso} value associated with the seventh site is reduced from −11.4 to 0.0. Notably, all the coupled spin states in Table 7 are associated with BS6 and the close matching of calculated and observed A_{iso} values allows us to definitively assign the four-coordinate Fe site as ferric: all other Fe sites are ferrous (see eq 1 and Tables 5 and 6).

Hyperfine values are also shown in Table 8 for states BS2 and BS7 (see Figure 10). For the spin coupling within BS7 and BS2 to be valid, the ferric site must be one of the three-coordinate Fe sites within the 4Fe′ cubane, notably different to

(61) (a) Kent, T. A.; Huynh, B. H.; Munck, E. *Proc. Natl. Acad. Sci. U.S.A.* **1980**, *77*, 6574. (b) Beinert, H.; Kennedy, M. C.; Stout, C. D. *Chem. Rev.* **1996**, *96*, 2335. (c) Gutlich, P.; Link, R.; Trautwein, A. *Mössbauer Spectroscopy and Transition Metal Chemistry*; Spring-Verlag: New York, 1978; pp 60−84. (d) Trautwein, A. *J. Phys. (Paris)* 1980, *41*, C1−95. (e) Shirley, D. A. *Rev. Mod. Phys.* **1964**, *36*, 339.

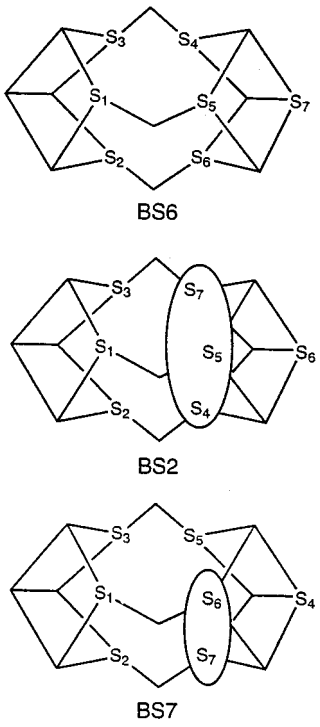

Figure 10. Location of spins in the vector coupling scheme for FeMoco. For BS6-1, BS6-2, and BS6-3, each spin vector is associated uniquely with one Fe site in each state and S_7 has a fixed location. For BS2, the three spin vectors (S_4, S_5, S_7, circled) can be interchanged and the ferric site S_7 can have different locations. For BS7, S_6, and S_7 (circled) can be interchanged.

BS6 where the ferric ion was four-coordinate. From eq 1 and Table 6, in BS2 the ferric site must appear within the spin triangle (Fe_6', Fe_7', or Fe_8'): in BS7 it must be either Fe_7' or Fe_6'. The ferric site (S_7) cannot however be associated with a specific Fe site and for each spin coupling scheme of BS2 the calculated A_{iso} values in Table 8 represent an average over the three possible positions of the ferric site. For BS7, calculated A_{iso} are averaged over the two possible ferric site positions (as shown in Figure 10, sites within the elliptical regions may be interchanged). The key point to emerge is that calculated A_{iso} values for BS2 and BS7 are a poorer match to the observed hyperfine A_{iso} values both in sign and in magnitude (even when spins are canted) than any of the calculated BS6 values.

3.8. Isomer Shift Correlation. The Mössbauer isomer shift (IS) is usually a good indicator of both oxidation state and metal ligand covalency, particularly when comparing related systems. From fundamental physical properties, the isomer shift is proportional to the total s electron density at the Mössbauer nucleus[61c−e] (the Fe sites of FeMoco). The measured s density at the nucleus is mainly altered by the electrostatic shielding of the s electrons (particularly core-type Fe 3s electrons) by the valence Fe 3d electrons. In addition, changes in the valence Fe 4s electron density can also alter the s electron nuclear density. Using all-electron DFT calculations, we have computed the total s electron density for a variety of 1Fe, 2Fe, and 4Fe sulfur complexes and used these to construct a linear correlation with measured Mössbauer isomer shifts.

Figure 11 shows one of two typical linear correlation plots of observed isomer shifts in synthetic model systems (filled symbols) versus calculated Fe electron density for the computational model systems of the type $Fe(SR)_n$ (n = 3, 4, SR = *S*-phenyl, $(SR)_2$ = S_2-*o*-xylyl) or $Fe_nS_n(SR)_4$ (n = 2, 4, R = phenyl). A similar slope and intercept is also obtained when

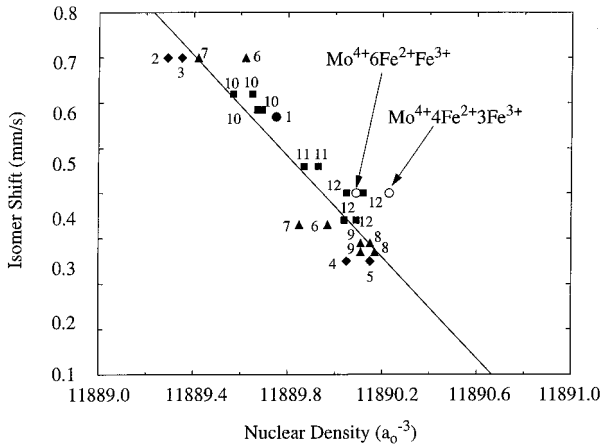

Figure 11. Typical correlation plot of calculated nuclear density versus observed isomer shift for model Fe−S systems. The plot shown corresponds to isomer shifts derived from a linear fit of 1Fe, 2Fe, and 4Fe S-phenyl and S_2-*o*-xylyl model compounds with available model compound data. Filled symbols correspond to: 1. $Fe(SC_6H_5)_3^{1-}$. 2. $Fe(SC_6H_5)_4^{2-}$.3.$Fe((SCH_2)_2(C_6H_4)_2^{2-}$.4.$Fe(SC_6H_5)_4^{1-}$.5.$Fe((SCH_2)_2(C_6H_4)_2^{1-}$. 6. $Fe_2S_2((SCH_2)_2(C_6H_4)_2^{3-}$. 7. $Fe_2S_2(SC_6H_5)_4^{3-}$. 8. $Fe_2S_2((SCH_2)_2(C_6H_4)_2^{2-}$. 9. $Fe_2S_2(SC_5H_5)_4^{2-}$. 10. $Fe_4S_4(SC_5H_5)_4^{3-}$. 11. $Fe_4S_4(SC_5H_5)_4^{2-}$. 12. $Fe_4S_4(SC_5H_5)_4^{1-}$. Open symbols represent $Mo^{4+}6Fe^{2+}Fe^{3+}$ and Mo^{4+}-$4Fe^{2+}3Fe^{3+}$ FeMoco.

Table 9. Calculated Nuclear Densities and ^{57}Fe Isomer Shifts ($mm\cdot s^{-1}$) for State BS6-1 (M^N, S = $^3/_2$, $Mo^{4+}6Fe^{2+}Fe^{3+}$) of the FeMoco Cluster

atom	nuclear density	IS[a]	IS[b]	expt.[c]	site	site type
Fe2	11890.02	0.37	0.35	0.33	B^1	Fe^{3+} cubane
Fe3	11890.17	0.28	0.27	0.50	B^2	Fe^{2+} triangle
Fe4	11890.12	0.31	0.30	0.41	A^4	Fe^{2+} triangle
Fe5	11890.30	0.21	0.20	0.33	B^1	Fe^{2+} triangle
Fe6	11889.93	0.42	0.40	0.39	A^1	Fe^{2+} cubane
Fe7	11890.05	0.35	0.33	0.48	A^2	Fe^{2+} cubane
Fe8	11890.08	0.34	0.32	0.39	A^3	Fe^{2+} cubane
average	11890.09	0.33	0.31	0.40		

[a] Isomer shifts (IS) derived from linear fit of 1Fe, 2Fe, and 4Fe S-phenyl and S_2-*o*-xylyl group model compounds with available model compound data.[60] [b] Isomer shifts derived from linear fit of 1Fe, 2Fe, and 4Fe S-phenyl and S_2-*o*-xylyl group model compounds with available protein data.[60] [c] Measured at 4.2 K for M^N state S = $^3/_2$.[21]

experimental Fe−S protein isomer shifts are used instead of isomer shifts from synthetic model complexes. The standard error for these fits varies between 0.05 and 0.06 $mm\cdot s^{-1}$, and correlation coefficients vary from $r = -0.94$ to -0.95. Details of the fitting procedure will be reported elsewhere.[60b] In Figure 11, by plotting the average experimental isomer shift against the average calculated nuclear densities for $Mo^{4+}6Fe^{2+}Fe^{3+}$ (Table 9) and $Mo^{4+}4Fe^{2+}3Fe^{3+}$ (Table S4), two points for FeMoco (open circles) are also incorporated into the figure. The $Mo^{4+}6Fe^{2+}Fe^{3+}$ point is closer to the line of best fit than the $Mo^{4+}4Fe^{2+}3Fe^{3+}$ alternative. Furthermore, the error associated with $Mo^{4+}6Fe^{2+}Fe^{3+}$ (the vertical distance from the open circle to the line, 0.07 $mm\cdot s^{-1}$) is similar to the error of the monomeric three-coordinate $Fe(SC_6H_5)_3^{1-}$ complex (0.05 $mm\cdot s^{-1}$); the corresponding error for the $Mo^{4+}4Fe^{2+}3Fe^{3+}$ oxidation state is much larger (0.15 $mm\cdot s^{-1}$).

Table 9 shows the results of applying the two fitting equations to the calculated electron densities at the Fe nuclei in our FeMoco model cluster. The state BS6-1 for M^N was calculated with $Mo^{4+}6Fe^{2+}Fe^{3+}$ as the oxidation state assignment. The average calculated IS (IS_{av} = 0.32 $mm\cdot s^{-1}$) is less than experimentally observed (IS_{av} = 0.40 $mm\cdot s^{-1}$), and the calculated

Table 10. Calculated and Experimental Average FeMoco ^{57}Fe Isomer Shifts (mm·s^{-1})

site type	system	Fe coord. no.	calculated IS		expt	
			fit to model data[a]	fit to protein data[b]	model	protein
Fe^{2+}	$Fe(SC_6H_5)_3^{1-}$	3	0.52	0.49	0.57	
Fe^{3+}	$Fe(SC_6H_5)_3^{0}$	3	0.28	0.27		
Fe^{2+}	$Fe(SC_6H_5)_4^{2-}$	4	0.78	0.73	0.70	0.68
Fe^{2+}	$Fe(S_2$-*o*-xylyl$)_2^{2-}$	4	0.74	0.70		
Fe^{3+}	$Fe(SC_6H_5)_4^{1-}$	4	0.35	0.33	0.25	0.24
Fe^{3+}	$Fe(S_2$-*o*-xylyl$)_2^{1-}$	4	0.30	0.28		
		Oxidation State $Mo^{4+}6Fe^{2+}Fe^{3+}$				
model compound interpolation[d]						
SC_6H_5-based fit			0.50	0.47		
directly calculated average IS						
SC_6H_5-based fit			0.33	0.31		0.40[c]
		Oxidation State $Mo^{4+}4Fe^{2+}3Fe^{3+}$				
model compound interpolation[e]						
SC_6H_5-based fit			0.43	0.40		
directly calculated average IS						
SC_6H_5-based fit			0.25	0.24		0.40[c]

[a] Using fit described in footnote a of Table 9. [b] Using fit described in footnote b of Table 9. [c] Reference 21, Expt. [d] Using calculated fit data and weighted average $6Fe^{2+}$(three-coordinate) + $1Fe^{3+}$(4-coordinate). [e] Using calculated fit data and weighted average $4Fe^{2+}$(three-coordinate) + $2Fe^{3+}$(three-coordinate) + $1Fe^{3+}$(four-coordinate).

isomer shift of $Mo^{4+}4Fe^{2+}3Fe^{3+}$ is even lower (IS_{av} = 0.23−0.25 mm·s^{-1}).

The proposed $Mo^{4+}4Fe^{2+}3Fe^{3+}$ oxidation state[21] for M^N was primarily based on a linear interpolation between the observed Mössbauer isomer shift of the only available synthetic 1Fe complex, $[Fe(SR)_3]^{1-}$ (R = 2,4,6-*t*-Butyl$_3$C$_6$H$_2$) (high-spin Fe^{2+}, IS = 0.57 mm·s^{-1}),[62] and also using estimated isomer shifts for the corresponding Fe^{3+} complex $[Fe(SR)_3]^0$, (high-spin Fe^{3+}, IS = 0.10−0.15 mm·s^{-1}) for which experimental data are not available. To test this linear interpolation proposal, the isomer shifts for the model complexes, $[Fe(SR)_3]^{1-/0}$ and $[Fe(SR)_4]^{1-}$ (R = phenyl), have been calculated, and the linear interpolation approach has been used to predict IS_{av} for the FeMoco (see Table 10). In accordance with the assigned oxidation states and coordination geometries, a weighted average of the $6Fe^{2+}$ (three-coordinate) and $1Fe^{3+}$ (four-coordinate) monomers was used for the $Mo^{4+}6Fe^{2+}Fe^{3+}$ case. For the $Mo^{4+}6Fe^{2+}Fe^{3+}$ state, this weighted average approach predicts an average isomer shift much higher than that directly calculated for the FeMoco. From our calculations, it appears that the linear interpolation procedure from three- and four-coordinate 1Fe complexes cannot reliably predict the isomer shifts of the more complicated polynuclear Mo7Fe cluster. The same conclusion is apparent for the $Mo^{4+}4Fe^{2+}3Fe^{3+}$ case (Table 10).

Table 10 also shows (both from our calculations and from experiment) that the local coordination geometry has a significant effect on isomer shift for the same metal oxidation state. Experimentally, the Fe^{2+} isomer shift changes from 0.70 mm·s^{-1} to 0.57 mm·s^{-1} when the Fe coordination changes from four- to three-coordinate.[22] The DFT calculated trend is similar but somewhat larger, changing from 0.78 to 0.52 mm·s^{-1}. The low isomer shifts calculated for the Fe^{2+} sites in FeMoco then arise due to the combined effects of their distorted three-coordinate geometry (as compared to a planar three-coordinate Fe^{2+} model complex) and the longer range environment which incorporates the novel Fe−Fe interactions. In contrast, the four-coordinate terminal capping Fe_2' (formally assigned as Fe^{3+} in FeMoco) is calculated to have a comparatively high isomer shift (0.34−0.37 mm·s^{-1}) and is generally higher than the calculated values for related monomeric Fe^{3+} sites (0.26−0.35 mm·s^{-1}) comparing Tables 9 and 10. This suggests that the Fe−S covalency in FeMoco is greater than in monomeric Fe^{3+} sites. Consequently, the four-coordinate Fe^{3+} isomer shift is predicted to be in the middle of the range of the three-coordinate Fe^{2+} sites in FeMoco. Overall, our isomer shift estimates, while not perfect, strongly suggest that a $Mo^{4+}6Fe^{2+}Fe^{3+}$ oxidation state assignment for M^N is indeed compatible with experiment, and that a more oxidized cluster assignment is not required.

3.9. M^N Oxidation Level 2: $Mo^{4+}4Fe^{2+}3Fe^{3+}$. To address the possibility that the $Mo^{4+}4Fe^{2+}3Fe^{3+}$ level might best represent M^N, additional BS calculations similar to those already implemented at the $Mo^{4+}6Fe^{2+}Fe^{3+}$ level have been performed for 12 alternative BS states in which two electrons have been removed from the FeMo cofactor. A starting point for the analysis is the initial assumption that the spin coupling scheme is developed from the $Mo^{4+}6Fe^{2+}Fe^{3+}$ oxidation state, such that the spins of the Fe sites are arranged in the following manner:

$$\begin{aligned} M_s(\text{total}) &= M_s(\text{3Fe Triangle}) + M_s(\text{4Fe}' \text{ Cubane}) \\ &= M_s(Fe_3 + Fe_4 + Fe_5) + M_s(Fe_2' + Fe_6' + Fe_7' + Fe_8') \\ &= (+2 - 2 - {}^5/_2) + (-{}^5/_2 + 2 + 2 + {}^5/_2) \\ &= {}^3/_2 \end{aligned} \quad (3)$$

As before, eq 3 depicts just one of a number of possible spin alignments, but each BS state satisfies the general M_s = $^3/_2$ spin requirement of the cluster and maintains the 4:3 pattern of site spins. All 12 BS states have been geometry optimized. Much of the analysis can be interpreted in a manner similar to that described above for the $Mo^{4+}6Fe^{2+}Fe^{3+}$ level. All supporting data are given in the Supporting Information.

Briefly, the calculated energies (Table S1) and associated geometries (Table S2) for the different BS states as well as the nature of the frontier orbitals changes little on two-electron oxidation. The BS6 states are low lying in both oxidation levels. The net spin densities (Table S3) reveal no spin associated with Mo (consistent with the ENDOR) but one unpaired electron resides on the homocitrate ligand. It therefore appears that the removal of two electrons from the Fe-based orbitals leaves the

(62) In the synthetic systems, the FeS_3 core is surrounded by bulky organic-based ligands, and although the coordination environment comprises three S-based ligands and therefore parallels that seen in FeMoco, the precise geometry is different.

Table 11. Average Bond Lengths[a] (Å) in Oxidized M^{OX}, Native M^N, Catalytically Reduced M^R and Radiolytically Reduced M^I FeMoco Clusters

	E^b	Mo−Fe	Fe−Fe	Fe−Fe′	Fe′−Fe′	Mo−S^3	Fe−S^2	Fe−S^3	Fe′−S^3	Mo−O	Mo−N
					Calculated						
M^{OX} ($S = 0$)	1.0	2.73	2.61	2.67	2.65	2.42	2.16	2.23	2.23	2.12	2.32
M^{OX} ($S = 1$)	0.4	2.73	2.62	2.73	2.63	2.43	2.18	2.23	2.24	2.12	2.33
M^{OX} ($S = 2$)	0.0	2.75	2.62	2.68	2.66	2.41	2.17	2.22	2.26	2.14	2.33
M^N		2.77	2.62	2.71	2.68	2.42	2.18	2.23	2.27	2.14	2.34
M^R	0.0	2.75	2.65	2.80	2.71	2.42	2.22	2.24	2.29	2.16	2.34
M^I	1.8	2.74	2.64	2.70	2.72	2.42	2.20	2.25	2.29	2.16	2.34
					Experiment						
oxidized 2.0 Å[c]		2.64	2.54	2.57	2.69	2.25	2.16	2.24	2.27	2.09	2.16
native Av 2.0 Å[d]		2.65	2.53	2.53	2.60	2.25	2.17	2.20	2.22	2.02	2.15
native (EXAFS)[e]		2.71	2.63	2.63	2.63	2.36	2.31	2.31	2.31	2.20	2.20
native Kp 1.6 Å[f]		2.69	2.64	2.61	2.67	2.34	2.21	2.24	2.24	2.32	2.48
reduced (EXAFS)[g]			2.66	2.60	2.60	2.60	2.36	2.33	2.33	2.33	2.13

[a] Reported X-ray data are averaged over both α subunits. [b] Gas-phase energy differences (kcal/mol). For the oxidized state, energies are relative to M^{OX} ($S = 2$). For the reduced state, energy of M^I is given relative to M^R. [c] Reference 13, PDB code: 2MIN(ox). [d] Reference 13, PDB code: 3MIN(red). [e] Reference 66. [f] Reference 17g, PDB code: 1QGU(red). [g] Reference 66.

FeMo cofactor highly oxidized and electron-deficient. To compensate, the Fe sites of the Mo7Fe9S core pull an electron from the homocitrate ligand.[63] Consequently, to maintain the $S = {}^3/_2$ spin state at the $Mo^{4+}4Fe^{2+}3Fe^{3+}$ level, the FeMo cofactor is best described in terms of spin $Mo^{4+}5Fe^{2+}2Fe^{3+}$ MoFe core having spin $S_{ab} = 2$ antiferromagnetically coupled to a spin $S_c = {}^1/_2$ homocitrate radical. Interestingly, recent analyses of steady-state EPR spectra of turnover samples for an acetylene-bound altered form (H195Q) of the MoFe protein[64] has revealed an unidentified radical signal suggested to arise from either the homocitrate or a closely lying glutamate or aspartate amino acid residue. Since the EPR is of an odd-electron state, prior to the two-electron transfer to the bound acetylene, FeMoco must be in the native oxidation state (E_0) or the two-electron reduced state (E_2). As this state can be formed during very low electron flux, E_0 may be more probable. The two-electron reduction of acetylene would presumably then leave the FeMo cofactor two electrons more oxidized than $Mo^{4+}6Fe^{2+}Fe^{3+}$ (formally now $Mo^{4+}4Fe^{2+}3Fe^{3+}$) and the existence of a homocitrate radical would agree with our calculations at the $Mo^{4+}4Fe^{2+}3Fe^{3+}$ level. However, this homocitrate radical state is not in agreement with EPR results for the resting state M^N.

3.10. Redox-Induced Changes in Geometry of FeMoco. The response of the geometry of the FeMo cofactor to the one-electron redox process is given in Table 11 for states M^{OX} ($S = 2$, 1, and 0[65]), M^N, M^R ($S = 2$) and M^I ($S = 1$). Regardless of whether the cluster becomes one-electron oxidized or one-electron reduced from M^N, the calculated differences in average bond length across all oxidation states are minor, suggesting the cluster is stable to one-electron redox events in either direction. The calculated average metal−metal separations show a slight lengthening on M^{OX} to M^N that is independent of spin state. A similar lengthening on further reduction to M^R or M^I is also calculated, contrary to the original EXAFS data,[66] which have been interpreted in terms of one-electron reduction causing a decrease in the volume of the cluster. The cluster is apparently large enough to accommodate the additional charge sufficiently well that the geometry remains largely unaffected, consistent with more recent measurements.[67a] The small expansion of the FeMo cofactor upon successive one-electron reduction is typically in accord with the behavior of polyhedral-type clusters that gain electrons.[67b]

Metal−metal interactions were noted previously for the resting state M^N to vary as a function of the spin state alignment pattern. Specific Fe−Fe distances are given in Table 12 for states M^{OX}, M^N, and M^R (and M^I) FeMo cofactors for a fixed-spin alignment pattern (BS6-1). As electrons and protons are added to the resting state, abrupt changes in the nature of the bonding may occur in more highly reduced states. A prelude to the overall effect is perhaps indicated by appearance of two short Fe−Fe interactions, 2.45 Å (intercubane interaction, delocalized Fe_3-Fe_8') and 2.48 Å (4Fe′ cubane, delocalized $Fe_6'-Fe_7'$), even in the absence of proton addition. The presence of such short Fe−Fe distances for M^I suggests that the Fe−Fe bonding could arise for the more highly reduced states of the FeMo cofactor; coupled protonation events may serve to enhance the effect. Evidence bearing on such issues will be reported in a future publication.

4. Conclusions

Spin polarized BS-DFT calculations have been used to find the oxidation state that best represents the M^N state of the FeMoco of nitrogenase and to provide a framework for the analysis of geometries, spectroscopy and energetics. The two

(63) Calculations on the dimethyl model at the $Mo^{4+}4Fe^{2+}3Fe^{3+}$ level do not result in the production of a methyl radical.

(64) (a) Sørlie, M.; Christiansen, J.; Dean, D. R.; Hales, B. J. *J. Am. Chem. Soc*. **1999**, *121*, 9457. (b) Sørlie, M.; Christiansen, J.; Lemon, B. J.; Peters, J. W.; Dean, D. R.; Hales, B. J. *Biochemistry* **2001**, *40*, 1540.

(65) (a) The $S = 0$ state for M^{OX} can be obtained in the following manner. Assuming the spin-coupling pattern in BS6-1 and all Fe sites are high-spin, from Figure 8, the Mo3Fe spin triangle has Fe sites with respective site spins of $Fe_3(\uparrow) = 2$, $Fe_4(\downarrow) = -2$, $Fe_5(\downarrow) = -2$, giving spin $S_a = -2$, while the 4Fe′ cubane has Fe site spins of $Fe_6'(\uparrow) = 2$, $Fe_7'(\uparrow) = 2$, $Fe_8'(\uparrow) = 2$ and $Fe_2'(\downarrow) = -{}^5/_2$ to give spin $S_b = {}^7/_2$. The antiferromagnetic coupling of $S_a + S_b$ gives the total spin of the cluster, $S_t = {}^3/_2$. The removal of one electron of majority spin from Fe_5 (for example) of the spin triangle yields the $S = 1$ M^{OX} state. The transition of a single electron from being minority spin-up on Fe_4 to minority spin-down on Fe_7' gives a state having an equal number of electrons and the following site spins: $Fe_3(\uparrow) = 2$, $Fe_4(\downarrow) = -{}^5/_2$, $Fe_5(\downarrow) = -{}^5/_2$, giving spin $S_a{}^{OX} = -3$, while the 4Fe′ cubane has Fe site spins of $Fe_6'(\uparrow) = 2$, $Fe_7'(\uparrow) = {}^3/_2$, $Fe_8'(\uparrow) = 2$ and $Fe_2'(\downarrow) = -{}^5/_2$ to give $S_b{}^{OX} = 3$. The important point is that Fe_7' (d^7) attains an intermediate site spin of $S = {}^3/_2$. The antiferromagnetic coupling of $S_a{}^{OX} + S_b{}^{OX} = -3 + 3 = 0$.

(66) (a) Christiansen, J.; Tittsworth, R. J.; Hales, B. J.; Cramer, S. P. *J. Am. Chem. Soc*. **1995**, *117*, 10017. (b) Chen, J.; Christiansen, J.; Tittsworth, R. J.; Hales, B. J.; George, S. J.; Coucouvanis, D.; Cramer, S. P. *J. Am. Chem. Soc*. **1993**, *115*, 5509. (c) Liu, H. I.; Filipponi, A.; Gavini, N.; Burgess, B. K.; Hedman, B.; Di Cicco, A.; Natoli, C. R.; Hodgson, K. O., *J. Am. Chem. Soc*. **1994**, *116*, 2418.

(67) (a) Strange, R. W.; Murphy, L. M.; Hasnin, S. S.; Gormal, C.; Eady, R. R.; Smith, B. E. Manuscript in preparation. (b) Cotton, F. A.; Wilkinson, G.; *Advanced Inorganic Chemistry*, 5th ed.; John Wiley and Sons: New York 1988. (c) Lanzilotta, W. N.; Seefeldt, L. C. *Biochemistry* **1997**, *36*, 12976. (d) Lanzilotta, W. N.; Christiansen, J.; Dean, D. R.; Seefeldt, L. C. *Biochemistry* **1998**, *37*, 11376.

Table 12. Fe−Fe Bond Lengths[a] (Å) in M^{OX}, M^N, M^R, and M^I FeMoco Clusters; for All States, the BS6-1 Spin Alignment Was Used

	M^{OX}			M^N	M^R	M^I	
	($S = 0$)	($S = 1$)	($S = 2$)	($S = {}^3/_2$)	($S = 2$)	($S = 1$)	M−M source
Fe_3-Fe_8'	2.53	2.59	2.54	2.57	2.58	**2.45**	intercubane
Fe_4-Fe_7'	2.78	2.87	2.84	2.85	2.95	2.85	Mo3Fe−4Fe′
Fe_5-Fe_6'	2.70	2.72	2.66	2.72	2.88	2.81	
expt.[b]		2.57[c]		2.53[d] (2.61)[e]	2.60[f]		
$Fe_2'-Fe_6'$	2.68	2.76	2.70	2.72	2.74	2.76	
$Fe_2'-Fe_7'$	2.66	2.56	2.65	2.66	2.70	2.75	
$Fe_2'-Fe_8'$	2.60	2.57	2.62	2.65	2.69	2.65	intracubane
$Fe_6'-Fe_7'$	**2.46**	2.54	2.60	2.57	2.58	**2.48**	4Fe′
$Fe_6'-Fe_8'$	2.58	2.57	2.60	2.59	2.60	2.65	
$Fe_7'-Fe_8'$	2.67	2.69	2.67	2.65	2.66	2.65	
Expt.[b]		2.69[c]		2.60[d] (2.67)[e]		2.60[f]	
Fe_3-Fe_4	2.67	2.66	2.67	2.67	2.68	2.67	intracubane
Fe_3-Fe_5	2.61	2.65	2.64	2.62	2.70	2.68	Mo3Fe
Fe_4-Fe_5	2.54	2.60	2.56	2.55	2.57	2.57	
Expt.[b]		2.54[c]		2.53[d] (2.64)[e]		2.60[f]	

[a] Short Fe−Fe distances are in bold (see text for a detailed discussion). [b] All experimental bond lengths denoted in the table represent an average over both α subunits for that bond type. [c] Oxidized *Av* protein at 2.0 Å resolution, PDB code: 2MIN(ox).[13] [d] Native *Av* protein at 2.0 Å resolution, PDB code: 3MIN(red).[13] [e] Native *Kp* protein at 1.6 Å resolution, PDB code: 1QGU(red).[17g] [f] Derived from EXAFS analysis of reduced *Av* protein.[66]

proposed oxidation states for M^N with formal metal-ion valencies of $Mo^{4+}6Fe^{2+}1Fe^{3+}$ and $Mo^{4+}4Fe^{2+}3Fe^{3+}$ have been compared. The principal conclusions from our calculations are:

(1) Analysis of both the iron and ligand hyperfine and Mössbauer isomer shifts favor the $Mo^{4+}6Fe^{2+}1Fe^{3+}$ as the correct oxidation state assignment for M^N. When the more oxidized $Mo^{4+}4Fe^{2+}3Fe^{3+}$ state is constructed, the metal-based core spontaneously oxidizes the bound homocitrate and produces a Mo^{4+}-$5Fe^{2+}2Fe^{3+}$-homocitrate radical state, which is incompatible with EPR and ENDOR observed for M^N. This state also gives much poorer Mössbauer isomer shift values compared to experiment for M^N. However, the $Mo^{4+}5Fe^{2+}2Fe^{3+}$-homocitrate radical state is a good candidate for the organic radical state observed by EPR[64] when acetylene is reduced during turnover conditions under low electron flux.

(2) Different possible spin couplings have been systematically constructed and compared to experiment with respect to optimized geometries, energies and properties of large FeMoco active site clusters. Of the 10 basic spin coupling alignments (Figure 4), the BS6 state spin alignment is preferred based on its geometry, metal-hyperfine coupling, and energy (after accounting for the protein and solvent energy term). For Mo^{4+}-$6Fe^{2+}1Fe^{3+}$, this state is composed of a Mo3Fe cluster with spin $S_a = 2$ AF coupled to a 4Fe′ cluster with spin $S_b = {}^7/_2$. This state has a significant analogy with the oxidized state (P^{OX}) of the 8Fe P cluster in the same protein.[18,53] In P^{OX}, the metal-ion valencies are $6Fe^{2+}2Fe^{3+}$, which can be further divided into two $3Fe^{2+}1Fe^{3+}$ sub-clusters. The total spin of $S = 4$ for P^{OX} arises from the ferromagnetic coupling of the two cubane halves, each having spins $S_1 = {}^1/_2$ and $S_2 = {}^7/_2$.[53a] The S_2 cubane of P^{OX} is then analogous to the S_b cubane of FeMoco, both in oxidation state and in spin alignment ($S_2 = S_b = {}^7/_2$).

(3) A significant argument in favor of the $Mo^{4+}6Fe^{2+}1Fe^{3+}$ oxidation state for M^N can be developed by comparing the active-site geometries, charges, and redox potentials of the $P^{SUPEROX} \rightarrow P^{OX}$, $P^{OX} \rightarrow P^N$, and $M^{OX} \rightarrow M^N$ redox couples. The $P^{OX} \rightarrow P^N$ redox couple is characterized by two successive, independent redox steps, $P^{OX} + 1e^- + 1H^+ \rightarrow P^{1+}$ and $P^{1+} + 1e^- \rightarrow P^N$, with redox potentials near −300 mV in *Av*; the $P^{SUPEROX} \rightarrow P^{OX}$ couple is a single-electron-transfer step of around +90 mV in the same protein; the $M^{OX} \rightarrow M^N$ redox couple of −42 mV in *Av* is more positive than the $P^{OX} \rightarrow P^N$ couple but more negative than the $P^{SUPEROX} \rightarrow P^{OX}$ potential.

From work on redox titrations of the P cluster by Lanzilotta et al.[67c,d] combined with the X-ray structures of Peters et al.,[13] the active-site charge of P^{OX} is either −4 (if both the bonded serine (Ser188b) side chain and amide (Cys88a) backbone are deprotonated) or −3 (if either Ser188b or Cys88a is deprotonated). Assuming the −3 form of P^{OX} for simplicity, the total charge of the P^N active site is −4. In contrast for M^N, the Mo^{4+}-$6Fe^{2+}1Fe^{3+}$ oxidation state implies that during the $M^{OX} \rightarrow M^N$ process, the total charges associated with M^{OX} and M^N are −1 and −2, respectively (not counting the terminal carboxylate charges of the homocitrate). The M center is about the same size as the P cluster (i.e., both contain eight metals), but the total cluster charges associated with the M center are lower, indicative of less electron−electron repulsion in the latter. Therefore, in principle, the redox potential for $M^{OX} \rightarrow M^N$ should be, and, is observed experimentally to be, more positive than $P^{OX} \rightarrow P^N$. From this perspective, if $Mo^{4+}4Fe^{2+}3Fe^{3+}$ were the correct oxidation state for M^N, the cluster charges corresponding to the $M^{OX}(Mo^{4+}3Fe^{2+}4Fe^{3+}) \rightarrow M^N(Mo^{4+}4Fe^{2+}$-$3Fe^{3+})$ redox couple would be +1 and 0, respectively. By analogy with the corresponding cluster charges of the P cluster, it is highly likely that the redox potential for $M^{OX} \rightarrow M^N$ at this oxidation level would be far more positive than the observed difference of 260 mV compared to the $P^{OX} \rightarrow P^N$ redox potential, and also more positive than the $P^{SUPEROX} \rightarrow P^{OX}$ couple in which the P cluster charges are −2 and −3, respectively. This argument is demonstrated quantitatively elsewhere.[53c]

(4) The predicted geometry of BS6 is a closer fit to the X-ray structures than the geometries from the BS7 and BS2 states. The RMSD fit for the $Mo7FeN_{His}S_{Cys}O_2$ core atoms improves as the X-ray structure becomes successively more refined from 2.2 to 2.0 to 1.6 Å, even though the initial starting geometry was taken from the 2.2 Å structure. Some very short Fe−Fe distances, 2.6 Å or less, are predicted by the calculations, consistent with the protein data. Nonetheless, the calculations indicate that Fe−Fe bonding is moderately weak (∼3 kcal/mol per Fe−Fe bond).

(5) The calculated Fe hyperfine A values for BS6 give a good fit to the experimentally observed hyperfine spectra from Mössbauer and ENDOR spectroscopies. Other low energy states, such as BS2 and BS7, give poorer Fe hyperfine A values and considerably larger spin densities at Mo, inconsistent with the negligible Mo hyperfine seen by ENDOR.

(6) The spin-coupled state BS6 has 3 distinguishable spin isomers, denoted BS6-1, BS6-2, and BS6-3, corresponding to three different locations for two down and one up spin vectors in the Mo3Fe subunit (Figure 7). These three isomers have very similar energies and their geometries fit the X-ray structures equally well. Similarly, the hyperfine fits are of nearly equal quality. However, BS6-1 shows a distinctive pattern for the spin-up and spin-down components of the LUMO (Figures 8 and 9). Qualitatively, these LUMO orbitals correspond well to those filled on $1e^-$ reduction, either catalytically during turnover, $M^N + 1e^- \rightarrow M^R(S = 2)$, or on radiolytic reduction, $M^N + 1e^- \rightarrow M^I(S = 1)$. Consistent with the observed changes in Mössbauer hyperfine properties and isomer shifts, the spin-up LUMO for M^R displays considerable Mo character and less Fe character within the Mo3Fe cubane; the spin-down LUMO for M^I is more delocalized across the central 3Fe−3Fe′ prismane (Figure 9).

(7) Our calculated changes in geometry for FeMoco are fairly small, both on one-electron oxidation to M^{OX} and one-electron reduction to M^R or M^I. Some Fe−Fe distances are calculated to shorten upon reduction to M^I, indicative of enhanced Fe−Fe bonding across some parallel spin pairs. Similarly, some Fe−Fe interactions are already short (<2.6 Å) for M^N, again, associated with pairs of parallel site spin vectors.

In general, the electronic, geometric, and spin-coupling structures and properties that we have calculated for M^N, M^{OX}, M^R, and M^I provide a good foundation for studying subsequent steps in the catalytic cycle. Our initial assessment of related charge distributions, the energetics of cluster interactions with the protein and solvent environment and redox potential calculations are presented elsewhere.[53c]

Acknowledgment. This work was supported by a NIH Grant to D.A.C. and L.N. (GM 39914). We thank Zhida Chen, Velin Spassov, Matthias Ullmann, Thomas Rod, Rhonda Torres, Wen-Ge Han, Michael Thompson, Brian Hales, Brian Hoffman, Eckard Münck, and Per Siegbahn for useful discussions. We also thank D. McRee for use of the Xtalview programs, E. Münck for providing data in advance of publication, and E.J. Baerends and the Amsterdam group for use of the ADF codes.

Appendix 1. Previous Theoretical Work

Deng and Hoffmann[33] utilized the extended Hückel method to calculate a cluster model $[HFe_4S_3(\mu-S)_3Fe_3S_3MoH_3]^-$ and concluded that metal−metal bonding in the cluster is important. They also considered nine possible N_2 binding modes. Stavrev and Zerner[34] employed the semiempirical ZINDO approach to study the whole FeMo cofactor, including side chain ligands to Mo and four coordination to Fe, but the calculations were done by the restricted open-shell Hartree−Fock (ROHF) approximation and a configuration-averaged method. They also explored various positions for nitrogen binding and found that N_2 preferentially coordinates inside the FeMo cofactor. Reduced forms of the FeMo cofactor were also examined with the contraction of the cluster and the change in Mo site upon reduction rationalized by bond index analysis.

The first density functional calculations on a large FeMo cofactor were done by Dance,[35] using a spin-restricted approach. He postulated another N_2 binding mode, in which the binding site is one of the Fe_4 quadrilateral faces of MoFe. Siegbahn et al.[36] published spin unrestricted hybrid density functional calculations on the mechanism of ammonia formation using a model cluster that was a more easily intelligible, approximate subunit of the full FeMo cofactor. Using an Fe(II)Fe(II) model as a starting point to study the N_2 binding and activation, the results were compared in few cases with a larger Fe_8S_9 model, for which no side ligands were included. However, only ferromagnetic coupling of the spins on the Fe sites was considered. Recently, Rod et al.[37] have studied the reactivity of FeMoco by using a plane wave basis set with a spin polarized exchange correlation functional. This study was based on a structure consisting of periodically repeating units, each with stoichiometric formula $MoFe_6S_9$. It was shown that N_2 can bind on top of FeMoco on one of the Fe sites and that a mechanism where adsorbed N_2 is hydrogenated stepwise to form two ammonia molecules is possible at low temperature, providing that the chemical potential of the reacting H atom is higher than that of H_2. The FeMoco calculations were also compared with corresponding calculations for a Ru(0001) surface and calculations for the Haber−Bosch mechanism on Ru(0001) to illustrate why two different mechanisms are in use, and that widely different reaction conditions are required for the enzyme and the metal surface. This study has recently been expanded.[38] The size of the FeMo cofactor employed has been extended to include a more correct description of the spin properties of the FeMo cofactor to rationalize a number of other experimentally observed features of FeMoco function, including H bonding and H_2 formation, CO adsorption, hydrogenation of adsorbed N_2, and proton transfer to adsorbed N_2 and CO. Of late, Morokuma et al.[39] have utilized hybrid (B3LYP) DF methods and examined various dinitrogen binding modes to Mo using an abbreviated model of the homocitrate end of the FeMo cofactor. In their approximate model, no Fe sites were included, and the principal conclusion was that His442 cannot be protonated at Nϵ.

In all cases, the reported calculations have provided considerable information but also share one or more of a number of shortcomings, neglecting several potentially vital aspects of the electronic structure. These include the use of structural models that are greatly oversimplified, model FeMo cofactors with d electron counts that are inconsistent with the available experimental data, the use of ferromagnetic rather than antiferromagnetic coupling of electron spins, and, a neglect of the protein/solvent environment; the latter contributes a number of essential features to the enzymatic function (as shown elsewhere).[53c] The protein environment has not been incorporated into any of these calculations (vide supra). Thus, the combined effect due to the charged amino acid side chains within the second ligand shell on the active site are not considered, as well as the potentially crucial role they play in hydrogen bonding, coupled electron/proton transfer, and stabilization of small molecule binding to the FeMo cofactor.

Appendix 2. Calculation of Fe Hyperfine Couplings

Observed Mössbauer and ENDOR ^{57}Fe hyperfine coupling parameters (A_i^{exp}) provide important information about the spin coupling structure in resting FeMoco with total spin $S = {}^3/_2$. To compare these hyperfine parameters with those derived from our computational model, the hyperfine coupling is represented as a product of three factors

$$A_i^{calc} = \bar{a}_i d_{B(i)} K_i^t \qquad \text{(A1)}$$

where i denotes the spin site, $\bar{a}_i$ is the *intrinsic site* hyperfine parameter for a purely ionic Fe site (an Fe^{3+} or Fe^{2+} ion), K_i^t is the spin projection parameter discussed below and $d_{B(i)}$ is a parameter that reflects metal−ligand covalency (when $d_{B(i)} = 1$, the site is purely ionic, and $d_{B(i)}$ decreases with increasing Fe−S covalency). As in earlier work,[53b] we find $d_{B(i)}$ from our DFT calculations based on the Fe(3d) Mulliken spin population on that Fe center, using

$$d_{B(i)} = \Delta P(Fe_i)/2S_i \quad \text{(A2)}$$

where $\Delta P(Fe_i) = P^{\alpha}(Fe_i) - P^{\beta}(Fe_i)$, and $P^{\alpha}(Fe_i)$ and $P^{\beta}(Fe_i)$ are the spin-up and spin-down Mulliken Fe 3d populations on that Fe center. S_i is the formal spin of that Fe center (here either Fe^{3+} or Fe^{2+}) so that $2S_i$ is the maximum number of unpaired electrons on that center (four for Fe^{2+} and five for Fe^{3+}).

The K_i^t are spin projection coefficients for projecting the site spin S_i onto the total system spin S_t. These factors account for the largest variations in observed hyperfine values among the different Fe sites. The method used for the spin coupling model here is a generalization of the one developed for four coupled spin vectors.[68a] It applies in the strong exchange coupling regime where Fe−Fe exchange coupling energies are larger than Fe site zero-field splitting terms. This is typically the case for iron−sulfur clusters. This method was applied to reduced $Fe_4S_4^{1+}$ clusters in reduced 4Fe ferredoxins and related synthetic models;[68a] closely related methods were used for analyzing ^{57}-Fe hyperfine coupling constants in 8Fe nitrogenase P-clusters (formally double cubane-type systems composed of two reduced Fe_4S_4 clusters coupled together but with a common sulfide corner atom).[66a] A general description of the theoretical framework and related applications is discussed elsewhere.[53b,68b]

In the present work, the system consists of seven spin vectors organized into two independent subsystems: the Mo3Fe (the Fe triangle) and the 4Fe cubane. The Mo ion is treated as low-spin ($S_{Mo} = 0$), as expected for the formally Mo^{4+} center and consistent with the small spin population seen on Mo (Tables 5 and 6) from the DFT calculations. The rationale for the decomposition into two subsystems is based both on mathematical simplicity and on the structure of the Fe−S−Fe linkages: only a single μS^2 bridge links each of the central prismane Fe sites to the neighboring Fe site on the other subunit. By contrast, within the 4Fe cubane, each Fe interacts with three other Fe sites, and within the 3Fe triangle, each Fe interacts with two other Fe sites. As shown in Figure 3, each of the six central prismane Fe sites is trigonally coordinated to sulfide, with two μS^3 sulfur bridges per Fe within the cubane and one intercubane μS^2 linkage. By contrast, the corner thiolate-bonded Fe of the Fe_4' cubane is linked to all other Fe centers within the cubane by two μS^3 bridge linkages from the corner Fe to each of the other Fe sites. Consistently, our calculations indicate that the strongest antiferromagnetic interactions involve this corner Fe site. The Fe 3d spin populations seen in the broken-symmetry calculations are consistent with the observation of a fairly reduced (mainly Fe^{2+} system), with the 3Fe triangle composed of $3Fe^{2+}$ and the 4Fe cubane composed of $3Fe^{2+}$ and $1Fe^{3+}$. From the approximate geometric symmetry and spin populations, the corner cubane Fe (bonded to cysteine thiolate) is assigned as the Fe^{3+} site for BS6 (see the main text).

For the calculation of hyperfine values at the Fe sites, the corresponding spin projection coefficients are needed. The 3Fe triangle is considered to have sites 1, 2, and 3 with total internal spin vector $S_a = S_{123}$, component spins S_1, S_2, and S_3, and intermediate spin S_{12}. The 4Fe cubane has total internal spin $S_b = S_{4567}$ composed of prismane-type spin sites $S_4S_5S_6$ and the terminal corner Fe site S_7 (For states BS2 and BS7, the ferric site S_7 is an internal three-coordinate Fe cubane site). Intermediate spin vectors S_{45} and S_{456} are also required. S_t (t = total) represents the total spin vector for the Mo7Fe system.

Since it is easy to miss the generality of the method and the conceptual framework in the detailed equations for this specific system, a simpler problem is first examined. Consider two spin vectors $\vec{S}_Q$ $\vec{S}_R$ coupled together so that $\vec{S}_Q + \vec{S}_R = \vec{S}_{QR}$. Then when S_Q, S_R, and S_{QR} are good quantum numbers, the expectation value of the scalar product of the vector operators $\langle \vec{S}_{QR} \cdot \vec{S}_Q \rangle$ is

$$\langle \vec{S}_{QR} \cdot \vec{S}_Q \rangle = [S_{QR}(S_{QR}+1) + S_Q(S_Q+1) - S_R(S_R+1)]/2 \quad \text{(A3)}$$

The spin projection coefficient is defined as the projection of the local spin vector S_Q on the total vector S_{QR}

$$K_Q^{QR} = \langle S_Q \rangle / \langle S_{QR} \rangle = \langle S_{QR} \cdot S_Q \rangle / \langle S_{QR} \cdot S_{QR} \rangle = \langle S_{QR} \cdot S_Q \rangle / S_{QR}(S_{QR}+1) \quad \text{(A4)}$$

The allowed spin quantum numbers for S_{QR} are $|S_Q - S_R| \le S_{QR} \le (S_Q + S_R)$. S_{QR} is always either integer or half-integer depending on the values of S_Q and S_R.[68c] In eq A4, S_Q can be the site spin or any composite spin; S_{QR} can be any composite spin assembled by coupling S_Q, S_R (including the total system spin S_t). With eqs A3 and A4, explicit spin projection coefficients can be found using the spin projection chain and sum rules. The spin projection chain rule follows directly from the use of eq A5

$$K_Q^{QRT} = [\langle S_Q \rangle / \langle S_{QR} \rangle][\langle S_{QR} \rangle / \langle S_{QRT} \rangle] = K_Q^{QR} K_{QR}^{QRT} \quad \text{(A5)}$$

which can be generalized to any number of successively coupled spins. To establish the sum rule, consider a set of site spins S_i which add up to a total spin S_t. Then

$$\sum_i K_i^t = \sum_i \langle \vec{S}_t \cdot \vec{S}_i \rangle / \langle \vec{S}_t \cdot \vec{S}_t \rangle = 1 \quad \text{(A6)}$$

This equation is valid for the total system, or for subsystems. For example, if there are two subsystems A, B, then $\sum_i K_i^A = 1$, $\sum_i K_i^B = 1$ (when i is restricted to each subsystem) and $K_A^t + K_B^t = 1$. With this background, we turn to the FeMoco cluster and first derive spin projection coefficients within the Fe triangle. From eq A5

$$K_1^{123} = K_1^{12} K_{12}^{123} \quad \text{(A7)}$$

Since all sites of the triangle are Fe^{2+}, $S_i = 2$, $K_1^{123} = K_2^{123}$, $K_1^{12} = {}^1/_2$, and K_{12}^{123} follows by substitution into eqs A3 and A4. Therefore

$$K_1^{123} = [S_{123}(S_{123}+1) + S_{12}(S_{12}+1) - S_3(S_3+1)]/[4S_{123}(S_{123}+1)] \quad \text{(A8)}$$

Using the sum rule eq A6 for the triangle

$$K_3^{123} = 1 - K_1^{123} - K_2^{123} \quad \text{(A9)}$$

Denoting 123 as subsystem A and 4567 as subsystem B, the final spin projection coefficients for subsystem A are determined by the spin quantum numbers above and by S_A, S_B, and S_t. Then for $i = 1, 2, 3$

$$K_i^t = K_i^A K_A^t \quad \text{(A10)}$$

and K_A^t is found using eqs A3 and A4.

The spin projection coefficients for the 4Fe cubane (subunit B) are evaluated by the same methods. Sites 4,5,6 are defined

(68) (a) Noodleman, L. *Inorg. Chem.* **1991**, *30*, 246. (b) Noodleman, L.; Peng, C. Y.; Case, D. A.; Mouesca, J.-M. *Coord. Chem. Rev.* **1995**, *144*, 199. (c) Brink, D. M.; Satchler, G. R. *Angular Momentum*, 2nd ed.; Oxford University Press: 1968. (d) Merzbacher, E. *Quantum Mechanics*, 2nd. ed.; New York: John Wiley and Sons: New York, 1970; pp 389−404.

as Fe^{2+} ($S_i = 2$) and the unique Fe^{3+} site is site 7. By direct analogy with eqs A7 and A8 for $i = 4,5$

$$K_4^{4567} = K_4^{45} K_{45}^{456} K_{456}^{4567} \tag{A11}$$

For site 7, and using eqs A3 and A4

$$K_7^{4567} = \langle \vec{S}_B \cdot \vec{S}_7 \rangle / [S_B(S_B + 1)] \tag{A12}$$

Alternatively, the left-hand sides of eqs A11 and A12 can be written as $K_4^B = K_5^B$ and K_7^B respectively. To find K_6^B, we again use the K sum rule

$$K_6^B = 1 - K_4^B - K_5^B - K_7^B \tag{A13}$$

As in eq A11, for $i = 4,5,6,7$

$$K_i^t = K_i^B K_B^t \tag{A14}$$

Then eqs A10 and A14 allow the evaluation of all spin projection coefficients for any given set of spin quantum numbers for the sites and composite spins.

Supporting Information Available: Example of an ADF input file for the HS state of $Mo^{4+}6Fe^{2+}1Fe^{3+}$ FeMoco; optimized coordinates for states (BS1−BS10, HS) of $Mo^{4+}6Fe^{2+}$-$1Fe^{3+}$ FeMoco; table of optimized relative energies (kcal/mol) of the 12 broken-symmetry spin alignments of FeMoco at the $Mo^{4+}4Fe^{2+}3Fe^{3+}$ level; table of comparison of calculated and experimental (averaged over the same bond type for $Mo^{4+}4Fe^{2+}$-$3Fe^{3+}$ FeMoco) geometries (Å and deg) for the three isomeric spin states of BS6; table of calculated Mulliken net spin population per atom for the $Mo^{4+}4Fe^{2+}3Fe^{3+}$ FeMoco cluster; table of calculated nuclear densities and ^{57}Fe isomer shifts ($mm \cdot s^{-1}$) for state BS6-1 (M^N, $S = {}^3/_2$, $4Fe^{2+}3Fe^{3+}$) of the FeMoco cluster (PDF). This material is available free of charge via the Internet at http://pubs.acs.org.

JA011860Y